Simulation of Flow and Mechanics in the Brain

Nadia Emilie Skoglund

Department of Mathematics
University of Bergen

This dissertation is submitted for the degree of
Master of Applied and Computational Mathematics

June 2019

Acknowledgements

I would like to thank my supervisors Florin Adrian Radu, Kundan Kumar and Ingeborg Gåseby Gjerde for their guidance and help. I am especially grateful for Ingeborg who has helped me considerably with both writing and coding. She has been an admirable supervisor, and I am very thankful for all her help in improving this thesis. Her tips regarding future work and corrections have been of great help and inspiration. Furthermore, I want to thank Florin for handing me this project and showing me how fun mathematics can be. I also want to thank Kundan for very helpful remarks and corrections. I really appreciate all the effort and help of all my supervisors.

PS: I would like to thank my co-students for lending me their textbooks throughout the year. It has also been a nice two years sharing the office with you.

Abstract

In this thesis, we study the numerical approximation solving a fully coupled quasi-static, linear Biot model in a 3D domain Ω with 1D line sources δ_Γ. To approximate the problem, we developed a scheme combining two techniques: (i) a splitting technique for solving the pressure and the flux and (ii) the fixed-stress splitting scheme. The scheme here is based on splitting the solution of both the pressure and the flux in the flow equations into one explicitly-known, low regularity term and one implicitly-unknown, high regularity term. The flow equations are then solved to get the high regularity terms. In the second step, the explicitly-known terms are interpolated onto the discrete space of the pressure and the flux. Thus, obtaining the reconstructed pressure and flux. Finally, to calculate the displacement by solving the mechanics equation with the actual pressure. This scheme has one additional step in comparison to the standard schemes. Optimal convergence were both theoretically and numerically proven for the novel scheme. Lastly, we simulated flow and mechanics for a data set describing a vascular system of a human brain to demonstrate simulations on a data set with complex geometry.

Introduction

There has been a growing interest for a model to solve fully coupled flow and mechanics in poroelastic media and this type of model has been extensively studied for decades. The main reason is the wide field of applications, for instance in geophysics and biomedicine. Some examples are: coupled flow and mechanics in soil science and civil engineering [Armero, 1999; Biot, 1941; Borja and Alarcón, 1995; Park, 1983; Schrefler, 2004; White and Borja, 2008], coupled heat flow and mechanics in mechanical engineering [Armero and Simo, 1992] and CO_2 sequestration [Morris, 2009a,b], i.e. the change in mechanical behavior as a result from injection of CO_2. There is also an interest in coupled flow and mechanics in bioengineering. In particular, the behavior of blood flow in soft-tissue systems, e.g. the brain.

The quasi-static, linear Biot model [Biot, 1941, 1955] was developed for studying poroelastic phenomena, and is the choice of mathematical model in this thesis. Moreover, the aim is to simulate flow and mechanics in the brain at the level of microcirculation. Therefore, a Dirac line source term is included in the right-hand side of the mass conservation equation, i.e. (1b). The system of equations read:

Find $(\boldsymbol{u}, p, \boldsymbol{w})$ such that:

$$-\nabla\cdot[2\,\mu\,\boldsymbol{\varepsilon}(\boldsymbol{u}) + \lambda\,(\nabla\cdot\boldsymbol{u})\,\boldsymbol{I}] + \alpha\,\nabla p = \boldsymbol{f}, \tag{1a}$$

$$\partial_t\left(\frac{p}{M} + \alpha\,\nabla\cdot\boldsymbol{u}\right) + \nabla\cdot\boldsymbol{w} = \psi + f\delta_\Gamma, \tag{1b}$$

$$\boldsymbol{K}^{-1}\,\boldsymbol{w} + \nabla p = \rho_f \boldsymbol{g}. \tag{1c}$$

The variables and parameters are as follows: $\boldsymbol{u}$ is the displacement, $\boldsymbol{\varepsilon}(\boldsymbol{u}) = \frac{1}{2}(\nabla\boldsymbol{u} + \nabla\boldsymbol{u}^T)$ is the (linear) strain tensor, p is the pressure, $\boldsymbol{w}$ is the flux, δ_Γ is the Dirac source term distributed on the line segment $\Gamma \subset \Omega \subset \mathbb{R}^3$, f is the intensity of the line source distributed on Γ, μ and λ are Lamé parameters, α is the Biot coefficient, $\boldsymbol{K}$ is the permeability tensor divided by the kinematic viscosity, ρ_f is the fluid density, M is the Biot modulus, $\boldsymbol{f}$ is the contribution from body forces, and ψ is a source term.

The Biot model, i.e. (1a)-(1c) with $f = 0$, are usually discretized in time by backward Euler, see e.g. [Both et al., 2017; Mikelić et al., 2014]. This is combined with a spatial-discretization method, where we mention the conformal finite element method for the mechanics and mixed finite element for the flow [Berger et al., 2017; Both et al., 2017; Phillips and Wheeler, 2007; Yi and Bean, 2016]. Other choices of spatial-discretization used for the Biot model is cell-centered finite volume [Nordbotten, 2016], mixed finite element method for both mechanics and flow [Yi and Bean, 2016], non-conforming finite element [Hu et al., 2017], MINI element [Rodrigo et al., 2016], continuous or discontinuous Galerkin [Chaabane and Rivière, 2018a,b] or multiscale methods [Castelletto et al., 2017, 2018; Dana and Wheeler, 2018].

In addition to the discretization methods for time and space, the Biot model can be solved by two alternatives: monolithically or with an iterative splitting algorithm. Solving the equations monolithically has the advantage of being unconditionally stable, but an iterative splitting algorithm is much easier to implement. Splitting the Biot model without adding a stabilization term leads to an unstable scheme [Kim et al., 2011]. Adding the stabilization term in the mechanics equations gives the undrained splitting scheme, and adding it in the flow equations gives the fixed-stress splitting scheme [Mikelić and Wheeler, 2013]. These splitting schemes are good alternatives for simulations of the linear Biot model since both schemes obtain good convergence rates, see e.g. [Berger et al., 2017; Kim et al., 2011; Mikelić and Wheeler, 2013]. In this thesis, we will consider the fixed-stress splitting scheme, which is a popular scheme in literature. The reason is its wide field of usage. Some examples of applications are: effectively solving the quasi-static, linear Biot model for poromechanics [Storvik et al., 2018], solving fully coupled quasi-static thermo-poroelasticity with nonlinear convective transport [Brun et al., 2019], Anderson acceleration for consolidation of unsaturated porous media [Both et al., 2019], non-linear extension of Biot's model for poromechanics [Borregales et al., 2018] and a space–time finite element approximation of the Biot system modeling fluid flow in deformable porous media [Bause et al., 2016]. Accordingly, in this thesis, (1a)-(1b) are discretized in time by using backward Euler and in space by the finite element method. The equations are then solved as a fully coupled, discrete system with the fixed-stress splitting scheme.

The line sources are interpreted as one-dimensional (1D) line segments in a three-dimensional (3D) domain. Mathematically, the line sources are modeled as Dirac distribution on the line segments [D'Angelo and Quarteroni, 2008]. This upscaling technique can be applied in various applications, e.g. modeling of 1D steel components in concrete structures [Llau et al.,

2016] or interference of metallic pipelines, bore-casings in electromagnetic concrete structures [Weiss, 2017] and interaction of a three-dimensional reservoir with the flow through 1D wells [Cerroni et al., 2019]. However, in the last years there has been an interest in using the same type of flow model for biological applications, e.g. studying blood flow in vascularized tissue of the brain [Grinberg et al., 2010; Reichold et al., 2009], efficiency of cancer treatment by hypothermia [Nabil and Zunino, 2016], and drug delivery through microcirculation [Cattaneo and Zunino, 2014; Possenti et al., 2018]. 1D line sources are good approximation when the radii of the roots, steel components, pipeline or blood vessel are negligible compared to their lengths and the size of the simulation domain. This upscaling technique causes the solutions to be singular, i.e. difficult to resolve numerically. It was proved that the lack of convergence is local to the area around the singularity (see [Gjerde et al., 2018; Köppl et al., 2016] and reference therein). Hence, we develop a singularity removal-based scheme on a splitting of the solutions of the pressure and the flux and the fixed-stress splitting scheme. [Gjerde et al., 2018] has shown that the splitting technique obtained optimal convergence when solving the following 3D flow model with 1D line sources:

$$-\nabla \cdot (\boldsymbol{K}\,\nabla p) = f\,\delta_\Gamma \qquad \text{in } \Omega, \tag{2a}$$

$$p \;=\; p_0 \qquad \text{on } \partial\Omega. \tag{2b}$$

In this thesis, the developed scheme is tested for solving the fully coupled Biot model. The splitting technique splits the solutions of the pressure and the flux into one (explicit) low regularity term denoted by the subscript s and one (implicit) high regularity term denoted with r [Gjerde et al., 2019]. The terms with the subscript s are known terms that captures the singularity of the solution. The splitting reads:

$$p = p_s + p_r, \tag{3a}$$

$$\boldsymbol{w} = \boldsymbol{w}_s + \boldsymbol{w}_r. \tag{3b}$$

(3a)-(3b) are used to reformulate (1b)-(1c) in order to solve the equations for the high regularity terms. The fixed-stress splitting scheme is then interpreted in three steps. Firstly, solving (1b)-(1c) for the updated p_r and $\boldsymbol{w}_r$. Secondly, interpolating p onto the discrete space of the pressure and thus obtaining the actual pressure. Lastly, (1a) with the reconstructed pressure from the previous step and then solved to get $\boldsymbol{u}$. This scheme will be referred to as the fixed-stress splitting scheme with singularity removal. It was developed for the purpose of simulating flow and mechanics at the level of microcirculation. To the best of our knowledge, simulating flow and mechanics in the brain have not been done before. At least not with

a 3D flow model with 1D line sources. The interest in simulating mechanics is motivated by vascular compliance. In biomedical applications, this is referred to as the relationship between the volume of the blood within a vascular vessel and the blood pressure generated by the presence of that volume. This property can help to determine diseases, e.g. vascular compliance is reduced in vascular dementia, but not in Alzheimer's disease [Dhoat et al., 2008].

Outline

Chapter 1 introduces basic theory used throughout the thesis. First, we introduce important concepts of single-phase flow in porous media. We here derive both Darcy's law and the mass conservation equation, which are two of our governing equations. In Section 1.2, we motivate the choice of mathematical model, where we mentioned that an upscaling technique is required to simulate flow and mechanics in the brain at the level of microcirculation. The chapter concludes with useful definitions. In particular, defining function spaces used for the variational formulation of (1a)-(1c), Green's functions used to aid in the approximation of the solutions and lemmas used for the convergence analysis.

In Chapter 2, we introduce our mathematical model. In Section 2.1, the quasi-static, linear Biot model is introduced and the mechanics equation (1a) is derived. In the next section, we introduce a splitting technique which has been proven to obtain optimal convergence for solving (2a)-(2b). We show the method when solving (2a)-(2.2b). The technique will be applied to (1a)-(1c) in Chapter 3 and 4.

We begin Chapter 3 by introducing the finite element method. Here, we introduce the conformal variational formulation with an example. Then we apply to (1a). Next, we introduce the mixed variational formulation, and apply it to (1b)-(1c). Lastly, in this section, Section 3.1.3 introduces the finite element discretization and Section 3.1.4 defines the discrete spaces used in our computations. We then introduce the iterative scheme. Section 3.2 first introduces our choice of time-discretization technique, i.e. backward Euler. Secondly, introducing the fixed-stress splitting scheme solving the Biot model, i.e. (1a)-(1c). Lastly, in this section, we introduce the fixed-stress splitting scheme with singularity removal. The scheme is based on the splitting of the solution of p and $\boldsymbol{w}$, i.e. (3a)-(3b). (1b)-(1c) are reformulated to solve for the high regularity terms, i.e. p_r and $\boldsymbol{w}_r$. The fixed stress splitting scheme is then interpreted to solve the reformulated flow equations and the mechanics equation in three steps. This is an additional step in comparison with the standard schemes. In the first step,

the reformulated flow equations are solved. Secondly, the low regularity terms, i.e. p_s and $\boldsymbol{w}_s$ are interpolated to the discrete spaces of the pressure and the flux, respectively, to obtain the actual pressure and flux. Lastly, we obtain $\boldsymbol{u}$ by solving the mechanics equation with the reconstructed pressure. This chapter concludes with a proof of convergence for this scheme.

In Chapter 4, we present our numerical results. We perform the convergence tests of the scheme introduced in Section 3.2.3, i.e. the fixed-stress splitting scheme with singularity removal. Here, we begin by performing convergence tests for three test cases where we set the parameters independent of z. Thus, we are only considering two dimensions. The first test problem was included as a reference case, where (1a)-(1c) with $f = 0$ are solved with the standard fixed-stress splitting scheme. Then, the second test case consisted of solving (1a)-(1c) with the standard fixed-stress splitting scheme, but ignoring a small region before calculating the errors. This demonstrated that the lack of convergence is mostly located in the area surrounding Γ. Finally, we numerically verified the theoretically results from Theorem 7 in Section 3.3. This means applying the fixed-stress splitting scheme with singularity removal, which was introduced in Section 3.2.3. After retrieving optimal convergence. We lastly simulated flow and mechanics for a data set describing a vascular system of a human brain.

Contributions

The contributions of this thesis are:

- Extending the Biot's equations to the case of including line sources.
- The dimensional gap causes the pressure to be singular. This makes it difficult to resolve numerically. Therefore, we combine two techniques to obtain optimal convergence. One splitting technique for solving flow problems in a 3D porous medium with 1D line sources, and second is the fixed-stress splitting scheme algorithm for the coupled flow and mechanics problem.
- Theoretical convergence proof of the fixed-stress splitting scheme with singularity removal for $d \in \{2,3\}$.
- Implementation of the novel numerical method developed here in FEniCS. Numerical experiments have been conducted that show errors and optimal convergence rates.
- Numerical tests on a real data set of a human brain to show application on a data set with complex geometry.

Table of contents

List of figures **xiii**

List of tables **xv**

List of symbols **xvi**

1 Basic theory **1**

1.1 Porous media 1

1.1.1 Porous media flow 1

1.1.2 Darcy's law 2

1.1.3 Conservation of mass 5

1.2 Flow and mechanics in the brain 6

1.3 Definitions 8

1.3.1 Function spaces 8

1.3.2 Green's function 10

1.3.3 Preliminaries 11

2 Mathematical modeling **13**

2.1 Biot's equations 14

2.2 Flow model with lower-dimensional source terms 15

2.2.1 Illustration of the method 16

2.2.2 Line sources 17

3 Discretization **21**

3.1 Finite element method 22

3.1.1 Conformal variational formulation 22

3.1.2 Mixed variational formulation 23

3.1.3 Finite element discretization 25

3.1.4 Discrete spaces 26

3.2 Iterative solver for Biot's equations 26
3.2.1 Backward Euler 27
3.2.2 Fixed-stress splitting scheme 28
3.2.3 Fixed-stress splitting scheme with singularity removal 29
3.3 Convergence analysis 31

4 Numerical simulations **38**
4.1 Numerical examples in 2D 39
4.1.1 Test case with smooth right-hand sides 40
4.1.2 Test case with a point source 42
4.1.3 Test case with a point source solved by the fixed-stress splitting scheme with singularity removal 47
4.2 Numerical simulations in 3D 50
4.2.1 Test case with a line source 51
4.2.2 Simulation of flow and mechanics in a non-trivial data set 55

5 Conclusions **58**
5.1 Future work 58

References **61**

List of figures

1.1 Illustration of a porous medium. 2
1.2 Illustration of Darcy's experiment. 3
1.3 A control volume with fluid and mass fluxes. 5
1.4 Illustration of an artery, a vein and a capillary. 7

2.1 Illustration of a blood vessel with a line segment $\Gamma = \{(0,0,z) : z \in [a,b]\}$ and its elongation $\tilde{\Gamma} = \{(0,0,z) \in \Omega\}$. R is a small region surrounding Γ with radius r. $P : \Omega \to \tilde{\Gamma}$ is a projection operator and projects a point in Ω onto the closest point on $\tilde{\Gamma}$. 18

3.1 Illustration of the triangle elements: Continuous Lagrange ($\mathbb{CG}_1$) (a), Discontinuous Lagrange ($\mathbb{DG}_0$) (b), and Raviart-Thomas ($\mathbb{RT}_0$) (c). The black dots and arrows indicate the degrees of freedom of the element. The subscripts denote the order of polynomials. 26

4.1 Numerical solutions obtained when applying the fixed-stress splitting scheme to a test problem with smooth right-hand sides: Pressure (a), magnitude of the flux (b), and magnitude of the displacement (c). 41
4.2 Illustration of the mesh size h of a triangle element (a), and the position of the point source with respect to the mesh (b). The uniform mesh is constructed by dividing the unit square into $1/h \times 1/h$ squares and dividing each square by the diagonal. The mesh size of the unit square mesh is the length of the shortest side of the triangle. 42
4.3 Upper line: Cropped plots of the pressure; analytic (a) and numerical (b). Lower line: Cropped plots of the magnitude of the flux; analytic (c) and numerical (d). These plots were obtained for a test problem solved by the fixed-stress splitting scheme with a point source. 45

4.4 Upper line: Plots of the pressure; analytic (a) and numerical (b). Middle line: Plots of the magnitude of the flux; analytic (c) and numerical (d). Lower line: Plot of the magnitude of the displacement; numerical (e). All plots are numerical solutions obtained by fixed-stress splitting scheme with a point source. 46
4.5 Upper line: Plots of the pressure; the low regularity term (a), the high regularity term (b) and the reconstructed pressure (c). Middle line: Plots of the magnitude of the flux; the low regularity term (d), the high regularity term (e) and the reconstructed flux (f). Lower line: Plot of the magnitude of the displacement; the displacement (g). All plots are numerical solutions obtained by fixed-stress splitting scheme with singularity removal with a point source. 49
4.6 Illustration of a tetrahedron element. The uniform cube is constructed by dividing the unit cube into $1/h \times 1/h \times 1/h$ cubes and dividing each cube by the diagonal. The mesh size for the unit cube mesh are the length of the shortest side of the tetrahedron. The red line illustrates a line source going through the center of the tetrahedron. 51
4.7 Upper line: Plots of the pressure; the high regularity term (a) and the reconstructed pressure (b). Middle line: Plots of the magnitude of the flux; the high regularity term (c) and the reconstructed flux (d). Lower line: Plot of the magnitude of the displacement; the displacement (e). All plots are numerical solutions obtained by fixed-stress splitting scheme with singularity removal with a line source. 54
4.8 Visualization of a vascular network of a human brain [Hodneland et al., 2019]. The red vessels illustrate arteries and the blue vessels illustrate veins. 55
4.9 Illustration of the data set describing a vascular system of the human brain: Front (a), side (b) and overview (c). Here, the arteries (red) and the veins (blue) and the data set consists of ~ 3000 line segments. It was constructed from a MRI scan [Tardif et al., 2016]. 55
4.10 The plots are obtained with a data set describing a vascular system of a brain: Contour plot of the pressure (a), magnitude of the flux (b), and the magnitude of the displacement (c). The results are found using the fixed-stress splitting scheme with singularity removal. The data set consists of line segments constructed from a MRI scan [Tardif et al., 2016]. The plots are cropped in ParaView after the simulations to fit the data set. 57

List of tables

4.1 Parameters for numerical examples in two dimensions. 40
4.2 Errors and convergence rates obtained when applying the fixed-stress splitting scheme to a test problem with all smooth variables. For reference, optimal convergence rates are listed in the bottom row. 41
4.3 Errors and convergence rates obtained with the fixed-stress splitting scheme to a test problem with a point source. Optimal convergence rates are listed in the bottom row. 43
4.4 Errors and convergence rates obtained with a point source. The results are obtained by solving the system of equations by the fixed-stress splitting scheme with singularity removal. Optimal convergence rates are listed in the bottom row. 48
4.5 Parameters for simulations in three dimensions. 50
4.6 Errors and convergence rates obtained with the fixed-stress splitting scheme with singularity removal to a test problem with a line source. The results are obtained with $\nu = 0.4999$, and $\mathbb{CG}_1$ elements for the displacements. Optimal convergence rates are demonstrated in the bottom row. 52
4.7 Errors and the convergence rates obtained with the fixed-stress splitting scheme with singularity removal to a test problem with a line source. Results obtained with $\mathbb{CG}_1$ elements and for $\nu = 0.4899$ [Zakerzadeh and Zunino, 2015]. The optimal convergence rate is demonstrated in the bottom row. . . 52
4.8 Errors and convergence rate for the displacement obtained with the fixed-stress splitting scheme with singularity removal to a test problem with a line source. Comparing the results obtained with $\mathbb{CG}_1$ and $\mathbb{CG}_2$ elements for $\nu = 0.4999$. 53

List of symbols

In this thesis, Δ denotes the Laplace operator, ∇ denotes the gradient, and $\nabla\cdot$ denotes the divergence. The relation $\Delta(\cdot) := \nabla\cdot\nabla(\cdot)$ will be used without further specification. Let the superscript T denote the transpose. For some variable k, let $\frac{\partial}{\partial k} = \partial_k$, $\frac{\mathrm{d}}{\mathrm{d}k} = \mathrm{d}_k$ and $\frac{\mathrm{d}^2}{\mathrm{d}k^2} = \mathrm{d}_{kk}$. Further, let the bold letters denote vectors and tensors. In plots, let letters with arrow above denote vectors. In the list of symbols, let M denote the mass unit, L denote the length unit, T denote the time unit, and F denote the force unit.

Greek symbols

α	Biot coefficient	–
$\bar{\Omega}$	Spatial domain $\Omega \cup \partial\Omega$	–
β_{FS}	Tuning parameter	–
δ_Γ	Dirac line source term	–
ε_a	Absolute error tolerance	–
ε_r	Relative error tolerance	–
Γ_j	Line segment j	–
λ	Lamé parameter	–
μ	Lamé parameter	–
μ_f	Dynamic viscosity	$\mathrm{FL}^{-2}\mathrm{T}^{-1}$
ν	Poisson's ratio	–
ν_f	Kinematic viscosity	$\mathrm{L}^2\mathrm{T}^{-1}$
Ω	Spatial domain	–

$\partial\Omega$	Boundary of spatial domain	–
ϕ	Porosity	–
$\boldsymbol{\varepsilon}(\cdot)$	(Linear) strain tensor	–
$\boldsymbol{\gamma}$	Normalized tangent vector of Γ	–
$\boldsymbol{\sigma}$	Cauchy stress tensor	–
$\boldsymbol{\sigma}^{por}$	Poroelastic Cauchy stress tensor	–
ψ	Source term	–
ψ_{sr}	Source term with singularity removal	–
ρ_f	Fluid density	ML^{-3}
τ	Time step size	T

Roman symbols

$\mathscr{T}_h$	Mesh discretization with mesh size h	–
$\mathfrak{t}$	Triangle	–
$\boldsymbol{a}$	Arbitrary point in $\Omega \subset \mathbb{R}^3$	–
$\boldsymbol{b}$	Arbitrary point in $\Omega \subset \mathbb{R}^3$	–
$\boldsymbol{f}$	Contribution from body forces in the porous media	F
$\boldsymbol{g}$	Gravitational acceleration vector	LT^{-2}
$\boldsymbol{K}$	Permeability tensor divided by ν_f	T
$\boldsymbol{k}$	(Intrinsic) permeability tensor	L^2
$\boldsymbol{n}$	Normal vector	–
$\boldsymbol{u}$	Displacement	L
$\boldsymbol{w}$	Mass flux	$\mathrm{ML}^{-2}\mathrm{T}^{-1}$
$\boldsymbol{w}_v$	Volumetric flux	$\mathrm{L}^3\mathrm{T}^{-1}$
d	Dimension	–

E	Bulk modulus	FL^{-2}
f	Dirac source term intensity	–
$f(s_j,t)$	Line source intensity of an arbitrary line segment j	–
$f(z,t)$	Line source intensity for a line segment $\Gamma = (0,0,z) \in \Omega \subset \mathbb{R}^3$	–
g	Gravitional acceleration constant	LT^{-2}
h	Mesh size	–
K	Permeability scalar divided by ν_f	T
M	Biot modulus	FL^{-2}
p	Fluid pressure	FL^{-2}
R	Region surrounding Γ	–
s_j	Arc-length of line segment j	L
T	Final time	T
t	Time	T

Superscripts

d	Dimension	–
i	Iteration level	–
n	Time level	–

Subscripts

a	Analytic solution	–
f	Fluid	–
h	Variable spatially discretized by h	–
R	Removal of region R	–
r	High (implicit) regularity term	–
s	Low (explicit) regularity term	–

Chapter 1

Basic theory

In this chapter, we will introduce basic theory which will be used in chapters to come, that is Chapter 2, 3 and 4. We start off by introducing basic concepts of single-phase flow in porous media. In particular, deriving two of our governing equations. In the second part, we motivate the choice of mathematical model for simulating flow and mechanics in the brain at the level of microcirculation. In the last part, we define basic function spaces used for calculations, Green's functions used to aid in the approximation of the solutions, and the lemmas used in the convergence analysis.

1.1 Porous media

We start this section by discussing single-phase flow in saturated porous media. We then move to derive two of our governing equations: first Darcy's law and then the mass conservation equation. We direct our theory towards the Biot's equations, which will be our mathematical model. The main source of this section is [Nordbotten and Celia, 2011], and we direct to [Nordbotten and Celia, 2011] for further theory of flow in porous media.

1.1.1 Porous media flow

A material with pores and a solid part is called a porous medium. The solid part is referred to as the matrix and the pores are referred to as the pore space. The pore space of the media can be filled with one or more gaseous or liquid fluids. The flow inside this media is referred to as a porous media flow. In this thesis, we will only consider single-phase flow. That is, a medium with a flow consisting of only one fluid. An example of a single-phase flow is water, and water and oil for a two-phase flow.

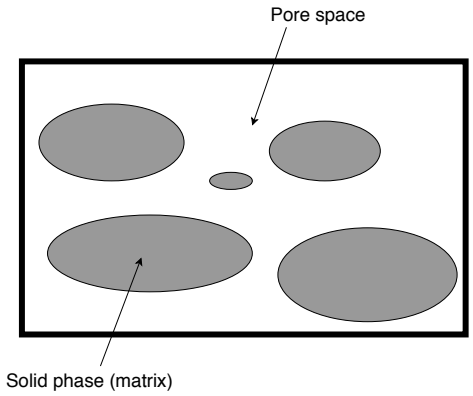

Fig. 1.1 Illustration of a porous medium.

Figure 1.1 illustrates the structure of a porous medium filled with one fluid. As denoted in the figure, the white area illustrates the pore space and the gray shapes illustrate the matrix. In a porous medium there only exists laminar flow, i.e. $Re << 1$. Re (Reynolds number) is a dimensionless quantity used to predict the pattern of the flow in different situations. The flow on this scale has a very complex geometry, where the quantities usually have characteristics of order 10^{-6}. Therefore, Representative Elementary Volume (REV) is introduced. REV is a length scale big enough to obtain defined averages over the pore space. In other words, the quantities considered in porous media are averages over the REV. The scale considered here is referred to as macro-scale. Darcy's law, which is derived in the next section, is only valid on macro-scale.

1.1.2 Darcy's law

One of the most important equations to describe flow in a porous medium is Darcy's law. We will derive Darcy's law for a single-phase flow in saturated porous media. The basis of the equation is experiments performed by Henry Darcy in 1856. The essence of the experiments is illustrated in Figure 1.2. As denoted in the figure, the cylinder is filled with sand and the tubes are filled with water. The cylinder will further be referred to as the column. Also, the lengths z_1 and z_2 are the heights where the tubes penetrate the column.

In general, the experiments consisted of predicting how much water that would flow through the sand filters. Darcy made several empirical observations from his experiments. The main observation was the following proportionality law

$$q \sim \frac{A\,(h_{f,2} - h_{f,1})}{\ell}. \tag{1.1}$$

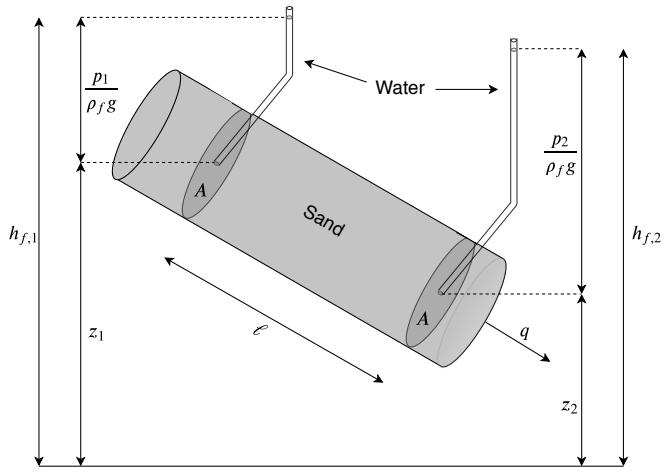

Fig. 1.2 Illustration of Darcy's experiment.

In words, Darcy's flux q is proportional to the cross-section A multiplied with the difference in hydraulic head $h_{f,2}$ and $h_{f,1}$ and divided by the column length ℓ. Darcy's flux is the volumetric flow rate through the column.

The first formulation of Darcy's law is obtained by introducing a proportionality coefficient κ in (1.1), i.e.

$$q = -\kappa \frac{A\,(h_{f,2} - h_{f,1})}{\ell}. \tag{1.2}$$

Here, κ will be referred to as the hydraulic conductivity. Darcy's law states that the fluid flows from regions with higher hydraulic head $h_{f,1}$ to regions with lower hydraulic head $h_{f,2}$. Hence, the minus sign in (1.2). This concept is generally for physical laws; where something is flowing from a region with high values to a region with low values, e.g. temperature flows from regions with high temperature to regions with low temperature. Moreover, Darcy found that κ was dependent on the sands' ability to transport fluid, i.e. the permeability of the sand. He found the following relationship between the hydraulic conductivity and the permeability:

$$\kappa = \frac{k\,\rho_f\,g}{\mu_f}. \tag{1.3}$$

In addition, k is the intrinsic permeability constant, ρ_f is the fluid density, g is gravitational acceleration constant and μ_f is the dynamic viscosity. Before extending Darcy's law to differential form, we introduce the volumetric flow rate per area w_v. The volumetric flow per area is obtained by dividing (1.2) by A, i.e.

$$w_v := \frac{q}{A} = -\kappa \frac{(h_{f,2} - h_{f,1})}{\ell}. \tag{1.4}$$

We will now extend Darcy's law to differential form. It is practical extending to three dimensions since real applications are in three dimensions. We start by treating the right-hand side of (1.4) as the differential of h_f. We assume that $\triangle h_f = h_{f,2} - h_{f,1}$ is small and further align the column along the z-axis. This means that $h_f = h_f(z)$. Under these assumptions, w_v can be rewritten as a one-dimensional differential:

$$w_v = -\kappa \, \mathrm{d}_z h_f. \tag{1.5}$$

Next, we extend $\mathrm{d}_z h_f$ to the gradient of h_f, i.e.

$$\nabla h_f \; = \partial_x h_f \, \boldsymbol{e}_x + \partial_y h_f \, \boldsymbol{e}_y + \partial_z h_f \, \boldsymbol{e}_z,$$

where $\boldsymbol{e}_j$ is the unit vector for coordinate $j = x, y, z$, respectively. Now, (1.5) can be extended to a three-dimensional vector:

$$\boldsymbol{w}_v = -\boldsymbol{\kappa} \, \nabla h_f, \tag{1.6}$$

where $\boldsymbol{\kappa}$ is the hydraulic conductivity tensor. We let the x-axis be in the horizontal direction. Then a general expression of the pressure along the column is given by

$$p = \rho_f g (h_f - z). \tag{1.7}$$

We rearrange (1.7) such that we obtain an expression for h_f:

$$h_f \; = \; \frac{p}{\rho_f g} \; + \; z. \tag{1.8}$$

Next, we insert (1.8) in (1.6), and remark that $\frac{\boldsymbol{\kappa}}{\rho_f g} = \frac{\boldsymbol{k}}{\mu_f}$ from (1.3). Then we have

$$\boldsymbol{w}_v \; = -\frac{\boldsymbol{k}}{\mu_f} \, (\nabla p \; + \; \rho_f \, g \, \nabla z), \tag{1.9}$$

where $\boldsymbol{k}$ is the intrinsic permeability tensor. Lastly, we insert $\boldsymbol{e}_z := \nabla z$ and $\boldsymbol{g} := -g \, \boldsymbol{e}_z$. This yields

$$\boldsymbol{w}_v \; = -\frac{\boldsymbol{k}}{\mu_f} \, (\nabla p \; - \; \rho_f \, \boldsymbol{g}), \tag{1.10}$$

which is the generalized three-dimensional formulation of Darcy's law for a single-phase flow. We now turn to derive our second governing equation, which is the mass conservation equation.

1.1.3 Conservation of mass

It is well-known in classical mechanics that mass is a fixed quantity, i.e. it cannot be formed or destroyed, but it can be deformed by an applied force. This means that in a closed system the total mass is conserved. In words, the general idea behind mass conservation for a control volume dV can be expressed as

$$\begin{pmatrix}\text{rate of change}\\ \text{of mass in d}V\end{pmatrix} = \begin{pmatrix}\text{mass flowing}\\ \text{into d}V\end{pmatrix} - \begin{pmatrix}\text{mass flowing}\\ \text{out of d}V\end{pmatrix} + \begin{pmatrix}\text{external mass}\\ \text{sources}\end{pmatrix}.$$

This is also illustrated in Figure 1.3.

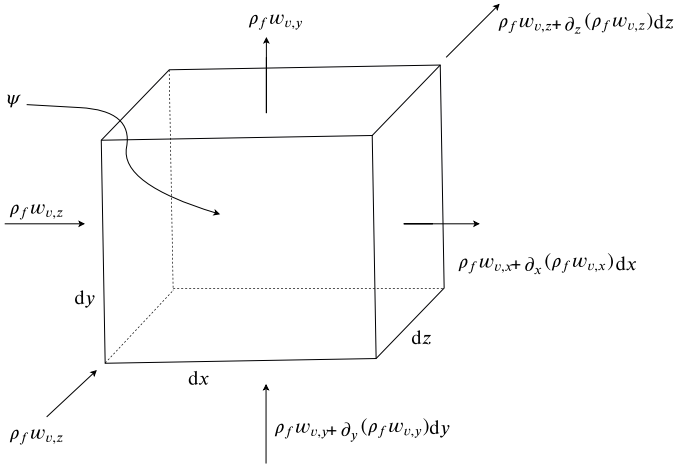

Fig. 1.3 A control volume with fluid and mass fluxes.

To derive the equation, we let $\mathrm{d}V = \mathrm{d}x\mathrm{d}y\mathrm{d}z$ and ψ be an external mass source. Then the mass flowing out of and inside of dV can be expressed as $-(\rho_f w_{v,j} + \partial_j\, \rho_f w_{v,j})$ and $\rho_f w_{v,j}$, respectively, where $j = x,y,z$. Next, we would like to express the rate of change of mass in dV. We let Φ be the total mass of the fluid in dV, where Φ can be expressed in terms of the porosity ϕ, the fluid density ρ_f, and the control volume dV. Then we have

$$\Phi = \rho_f \phi \mathrm{d}V. \tag{1.11}$$

The porosity is defined as the ratio between the volume of the pore space V_p and the total volume V of the porous medium, i.e.

$$\phi \;=\; \frac{V_p}{V}.$$

Moreover, we let dt be a small time-interval. Then the mass conservation equation can be written as

$$\partial_t \Phi \, \mathrm{d}t = \rho_f w_{v,j} \mathrm{d}t - (\rho_f w_{v,j} \mathrm{d}t + \partial_j \, \rho_f w_{v,j} \, \mathrm{d}V \mathrm{d}t) + \psi \, \mathrm{d}V \mathrm{d}t. \tag{1.12}$$

Next, we expand for all components and insert (1.11) in (1.12). This yields

$$\begin{aligned} \partial_t(\rho_f \phi \mathrm{d}V) \, \mathrm{d}t \; &= - \, \partial_x(\rho_f w_{v,x}) \, \mathrm{d}x \, \mathrm{d}y \, \mathrm{d}z \, \mathrm{d}t \\ &- \, \partial_y(\rho_f w_{v,y}) \, \mathrm{d}y \, \mathrm{d}z \, \mathrm{d}x \, \mathrm{d}t \\ &- \, \partial_z(\rho_f w_{v,z}) \, \mathrm{d}z \, \mathrm{d}x \, \mathrm{d}y \, \mathrm{d}t \\ &+ \, \psi \, \mathrm{d}x \, \mathrm{d}y \, \mathrm{d}z \, \mathrm{d}t. \end{aligned}$$

Further, we assume that the control volume is fixed in time, i.e. d$V = const.$. Then the final form of the mass conservation equation reads

$$\partial_t(\rho_f \phi) \; + \; \nabla \cdot (\rho_f \boldsymbol{w}_v) \; = \; \psi. \tag{1.13}$$

So far, we have derived Darcy's law and the mass conservation equation. In addition to this, we introduced some important properties for flow in porous media. Before turning to function spaces, and defining some useful lemmas, we will introduce some physical properties of flow and mechanics in the brain. We also here motivate the choice of mathematical model.

1.2 Flow and mechanics in the brain

There are numerous fields where simulation of flow and mechanics in a porous medium are of interest. Some examples are CO_2 storage, water and soil pollution, nuclear waste management and cancer research (in particular tumor growth). A popular mathematical model for solving fully coupled flow and mechanics equations in a poroelastic medium is the quasi-static, linear Biot model [Biot, 1941, 1955]. This model will be discussed in Section 2.1, and consists of a system of three equations solving for pressure, flux, and displacement. It was developed for studying poroelastic phenomena, i.e. describing the interaction between the deformation of an elastic porous medium and the fluid flow inside.

In addition to the Biot model, we need an upscaling technique to simulate flow and mechanics in the vascular system of the brain. The structure of the vessels at the level of microcirculation

has very complex geometry. These networks consist of thousands of vessels. Figure 1.4 illustrates an example of the structure of a capillary and also captures the differences in the radii of arteries, veins, and capillaries. A capillary vessel has a radius of approximately $4\mu m$ [Støverud et al., 2012]. Hence, it would be computationally intractable to resolve these vessels as 3D objects in the mesh. Consequently, we need to upscale the flow equations.

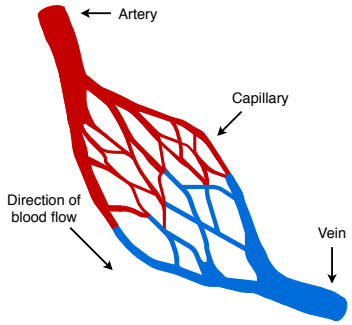

Fig. 1.4 Illustration of an artery, a vein and a capillary.

A popular upscaling technique is homogenization. In this technique, the brain and the vascular system are considered two different porous media [Dewhirst and Secomb, 2017; Shipley and Chapman, 2010], where Darcy's law is used to calculate the pressure and flux [Helmig, 1997; Khaled and Vafai, 2003]. Though this reduces the computational costs and the data volume, both the pressure and the flux can only be expressed as averages over the control volume. A requirement of homogenization is that the medium is periodic, but since the vessels at the level of microcirculation has very complex geometry, it is not certain that it can be described as a periodic medium. For this reason, another upscaling technique was developed with this application in mind. Here, the blood vessels are reduced to one-dimensional (1D) line segments [D'Angelo and Quarteroni, 2008], where the surrounding tissue is modeled as a three-dimensional (3D) porous medium. This technique is applicable since the radii of the blood vessels are very small compared to their lengths and the size of the simulation domain. The drawback of this reduction technique, is that it causes the solutions to be singular. Consequently, the solutions are difficult to resolve numerically. In particular, it leads to suboptimal convergence [Gjerde et al., 2018; Köppl et al., 2016]. One way to obtain optimal convergence rates is to split the solutions of the pressure and flux into one low regularity term and one high regularity term [Gjerde et al., 2018]. This terminology will be explained later in Section 2.2, and will be applied to the Biot model with lower-dimensional source terms in Chapter 3 and 4.

The Biot model has been studied extensively, see e.g. [Bause et al., 2016; Berger et al., 2017; Hu et al., 2017; Rodrigo et al., 2018; Showalter and Momken, 2002; Yi, 2017]. This

model is suitable for simulation of flow and mechanics in the brain since the blood vessels are poroelastic. To the best of our knowledge, the Biot model has not been coupled with a 3D flow model with 1D line segments to simulate flow and mechanics at the level of the microcirculation. In this thesis, we will develop numerical methods to approximate this type of problem. There is a lot of literature for dealing with the flow and transport in the brain, see e.g. [Dewhirst and Secomb, 2017; Penta et al., 2014; Shipley and Chapman, 2010]. Though there is also an interest to study the mechanics in the brain. The interest in simulating mechanics in the brain is motivated by vascular compliance. This is a relationship between the volume of the blood within a vascular vessel and the blood pressure generated by the presence of that volume, and can be applied to biomedical application. It can be of help when determining diseases. One example is that vascular compliance is reduced in vascular dementia, but not in Alzheimer's disease [Dhoat et al., 2008].

1.3 Definitions

Finally, this chapter will conclude with defining general function spaces used for solving the Biot model and Green's functions used to aid in the splitting technique introduced in Section 1.2. Lastly, we included some useful lemmas used in the convergence analysis.

1.3.1 Function spaces

We start off by defining weak derivatives. Note that [Evans, 2010] is the main source for the definitions to come. We let $C_c^\infty(\Omega)$ be the space of infinity differentiable functions $v : \Omega \to \mathbb{R}$ with compact support in Ω, i.e. the values map to zero near the boundary $\partial\Omega$. We assume that we have the two functions $u \in C^1(\Omega)$ and $v \in C_c^\infty(\Omega)$. From partial integration, we have weak derivatives of v if

$$\int_\Omega u_{x_i}\, v \,\mathrm{d}x = -\int_\Omega u\, v_{x_i} \,\mathrm{d}x. \tag{1.14}$$

The boundary term was excluded since, as stated, v has compact support on Ω. Next, we define four function spaces. Note that a Banach space is a complete, normed linear space. Also, a space is said to be complete if every Cauchy sequence in the space is convergent to a point in the space [Cheney, 2001]. Before turning to the definitions of the function spaces, we define an operator D. Let $\boldsymbol{\alpha} = (\alpha_1, \ldots, \alpha_n)$ be a multiindex of order $|\boldsymbol{\alpha}| = \alpha_1 + \ldots + \alpha_n = m$ for $1 \leq m \leq \infty$. Then

$$D^{\boldsymbol{\alpha}} v = \frac{\partial^{\alpha_1}}{\partial x_1^{\alpha_1}} \cdots \frac{\partial^{\alpha_n}}{\partial x_1^{\alpha_n}} v.$$

We also introduce the short-hand notations for the inner product and the induced norm

$$\langle u\, v\rangle_{L^2(\Omega)} = \langle u, v\rangle, \quad \|u\|_{L^2(\Omega)} = \|u\|_{L^2} = \|u\|,$$

respectively. Now, we define the function spaces:

Definition 1.1. *A Hilbert space H is a Banach space equipped with an inner product which generates the norm with respect to the function space.*
a. *The space $L^2(\Omega) = H^0(\Omega)$ is a Hilbert space with*

$$\langle u, v\rangle = \int_\Omega u\, v\, dx,$$

for $u, v \in L^2(\Omega)$.
b. *The Sobolev space $H^m(\Omega)$ is a Hilbert space where*

$$u \in H^m(\Omega),$$

there exists

$$D^{\boldsymbol{\alpha}} u \in L^2(\Omega),$$

such that

$$\int_\Omega D^{\boldsymbol{\alpha}} u\, v\, dx = (-1)^{|\boldsymbol{\alpha}|} \int_\Omega u\, D^\alpha v\, dx, \quad \forall v, D^{\boldsymbol{\alpha}} v \in L^2(\Omega).$$

c. *The Sobolev space $H(div;\Omega)$ is a Hilbert space where*

$$u \in H(div;\Omega)$$

implies

$$D^{\boldsymbol{\alpha}} u, \nabla \cdot u \in L^2(\Omega).$$

d. *Let Ω be bounded and $\partial\Omega$ be C^1. Then there exists a bounded linear operator T:*

$$T : H^1(\Omega) \to L^2(\partial\Omega),$$

where a function $u \in H_0^1(\Omega)$ is said to have zero-trace if and only if

$$Tu = 0 \quad \text{on } \partial\Omega.$$

Definition 1.2. *Let $C^0(\bar{\Omega})$ be the space of continuous function $u : \bar{\Omega} \to \mathbb{R}$, where u is zero-times continuous differentiable and $\bar{\Omega} = \Omega \cup \partial\Omega$.*

1.3.2 Green's function

Modeling the blood vessels as 1D line segments lead to a great reduction of the computational complexity of the model as it avoids expensive meshing of the blood vessels. As stated in Section 1.2, the model reduction has the drawback of inducing the solutions to be singular. Consequently, they become difficult to resolve numerically. To avoid this, we introduce a splitting technique [Gjerde et al., 2018] for the solutions. The splitting technique relies on the use of Green's functions in order to capture the singularity. Therefore, let us introduce the Green's functions. The need of Green's functions will be made clearer with the discussion of a 3D flow model with 1D line source terms in Section 2.2.

We start with letting a line segment $\Gamma = (0,0,z) \in \Omega$ pass through entire domain $\Omega \subset \mathbb{R}^3$ and (r,θ,z) be the cylindrical coordinates with $r = \sqrt{x^2+y^2}$. Then the Green's function for the Laplacian $-\Delta$ in $\mathbb{R}^3$ is given by

$$G(r) = -\frac{1}{2\pi}\ln(r), \tag{1.15}$$

where $G(r) \in L^2(\Omega)$ and $1/2\pi$ is a scaling factor. If we let δ_Γ be the Dirac line source distributed on the line segment $\Gamma \subset \Omega \subset \mathbb{R}^3$. Then the fundamental property of $G(r)$ is given by

$$-\int_\Omega \Delta G(r)\ v\ \mathrm{d}\Omega = \int_\Omega v\ \delta_\Gamma\ \mathrm{d}\Omega = \int_\Gamma v\ \mathrm{d}S \qquad \forall v \in C^0(\bar{\Omega}), \tag{1.16}$$

where $\mathrm{d}S$ is an element on Γ. Moreover, we now let $\Gamma \subset \Omega$ be an arbitrary line segment and $\Omega \subset \mathbb{R}^3$. Then the Green's function for the Laplacian $-\Delta$ in $\mathbb{R}^3$ is given by

$$G_{3D}(\boldsymbol{x},\boldsymbol{y}) = \frac{1}{4\pi}\frac{1}{\|\boldsymbol{x}-\boldsymbol{y}\|}, \tag{1.17}$$

where $G_{3D} \in L^2(\Omega)$. In the case of an arbitrary line segment, we seek the candidate $G(\boldsymbol{x})$ such that it solves

$$-\Delta G(\boldsymbol{x}) = \delta_\Gamma \qquad \text{in } \Omega, \tag{1.18}$$

where δ_Γ is a Dirac line source distributed on a line segment $\Gamma \subset \Omega \subset \mathbb{R}^3$. The (implicit) high regularity term in the splitting of the solutions corrects the lack of boundary conditions for solving (1.18). $G(\boldsymbol{x})$ is obtained by the convolution of δ_Γ and (1.17). The convolution of two functions $u(x)$ and $v(x)$ is defined as

$$(u * v)(x) := \int u(x-\gamma)\ v(\gamma)\ \mathrm{d}\gamma,$$

where $*$ is the convolution operator. We then obtain $G(\boldsymbol{x})$:

$$\begin{aligned} G(\boldsymbol{x}) &= \delta_\Gamma * G_{3D} \\ &= \frac{1}{4\pi}\int_\Omega \frac{\delta_\Gamma}{\|\boldsymbol{x}-\boldsymbol{y}\|}\mathrm{d}\boldsymbol{y} \\ &= \frac{1}{4\pi}\int_\Gamma \frac{1}{\|\boldsymbol{x}-\boldsymbol{y}\|}\mathrm{d}S. \end{aligned} \tag{1.19}$$

The fundamental property of $G(\boldsymbol{x})$ is given by

$$-\int_\Omega \Delta G(\boldsymbol{x})\, v \,\mathrm{d}\Omega = \int_\Omega v\ \delta_\Gamma \,\mathrm{d}\Omega = \int_\Gamma v \,\mathrm{d}S \qquad \forall v \in C^0(\bar{\Omega}). \tag{1.20}$$

1.3.3 Preliminaries

In this section, we included the lemmas used in the convergence analysis in Section 3.3. They read:

Lemma 1 (Polarization identity)**.** *Let $(X, \langle\cdot,\cdot\rangle_X)$ be a Hilbert space and $u, v \in X$. Then it holds*

$$\langle u, v\rangle_X = \frac{1}{4}\|u+v\|_X^2 - \frac{1}{4}\|u-v\|_X^2 .$$

Lemma 2 (Binomial identity)**.** *Let $(X, \langle\cdot,\cdot\rangle_X)$ be a Hilbert space and $u, v \in X$. Then the following inequality holds*

$$\langle u-v, v\rangle_X = \frac{1}{2}\|u\|_X^2 + \frac{1}{2}\|u-v\|_X^2 - \frac{1}{2}\|v\|_X^2 .$$

Lemma 3 (Cauchy-Schwarz inequality)**.** *Let $(X, \langle\cdot,\cdot\rangle_X)$ be a Hilbert space and $u, v \in X$. Then the following estimate holds*

$$|\langle u, v\rangle_X| \le \|u\|_X^2 \|v\|_X^2 .$$

Lemma 4 (Young's inequality)**.** *Let $a, b, \varepsilon \in \mathbb{R},\ \varepsilon > 0$. Then*

$$|ab| \le \frac{1}{2\varepsilon}a^2 + \frac{\varepsilon}{2}b^2.$$

Lemma 5 (Arithmetic Mean-Root-Mean Square (AM-RMS) inequality)**.** *Let $m \in \mathbb{N}$ and $\{u_j\}_{j=1}^m \subset \mathbb{R}$. Then the following inequality is true*

$$\frac{1}{m}\sum_{j=1}^m u_j \le \sqrt{\frac{1}{m}\sum_{j=1}^m u_j^2}.$$

Lemma 6 (Thomas' Lemma [Radu, 2004; Thomas, 1977])**.** *There exists a constant $C_{\Omega,d} > 0$ not depending on the mesh size h, such that given an arbitrary $q_h \in Q_h$, there exists $\boldsymbol{z}_h \in \boldsymbol{Z}_h$, satisfying $\nabla \cdot \boldsymbol{z}_h = q_h$, and $\|\boldsymbol{z}_h\| \leq C_{\Omega,d} \|q_h\|$.*

Chapter 2

Mathematical modeling

In this chapter, we will introduce our mathematical model. We consider the quasi-static, linear Biot model to simulate flow and mechanics in the vascular system of the brain. The Biot model includes 1D line sources in the right-hand side of the mass conservation equation. The choice of model was motivated in Section 1.2. The system of equations read:

$$-\nabla \cdot [2\mu \boldsymbol{\varepsilon}(\boldsymbol{u}) + \lambda \ (\nabla \cdot \boldsymbol{u}) \ \boldsymbol{I}] + \alpha \nabla p = \boldsymbol{f}, \tag{2.1a}$$

$$\partial_t \left(\frac{p}{M} + \alpha \ \nabla \cdot \boldsymbol{u} \right) + \nabla \cdot \boldsymbol{w} = \psi + f \delta_\Gamma, \tag{2.1b}$$

$$\boldsymbol{K}^{-1} \ \boldsymbol{w} + \nabla p \ = \rho_f \boldsymbol{g}. \tag{2.1c}$$

In addition, (2.1a) is the mechanics equation, (2.1b) is the mass conservation equation and (2.1c) is Darcy's law. In the first section, we introduce the Biot model (2.1a)-(2.1c), i.e. $f = 0$. Furthermore, [Gjerde et al., 2018] suggested a mathematical technique to obtain optimal convergence for solving:

$$-\nabla \cdot (\boldsymbol{K} \ \nabla p) = f \delta_\Gamma \qquad \text{in } \Omega, \tag{2.2a}$$

$$p \ = \ p_0 \qquad \text{on } \partial\Omega. \tag{2.2b}$$

We observe that (2.2a) is the same as (2.1b) with additional terms. The goal of Section 2.2 is to introduce a mathematical approach which obtains optimal convergence for solving (2.2a)-(2.2b). We will apply this technique to (2.1b)-(2.1c) in Chapter 3 and 4.

2.1 Biot's equations

We start off by introducing the fully coupled quasi-static, linearized Biot system, i.e. (2.1a)-(2.1c) with $f = 0$. Recall Darcy's law and the mass conservation equation were derived in Section 1.1. We will first derive the first governing equation, that is the mechanics equation (2.1a). Next, we apply some manipulations to the last two equations.

An important property in the derivation of (2.1a) is poroelasticity, which was mentioned in Section 1.2. Poroelasticity is used to describe the elastic behavior of a material with pore networks where there exists a pressurized fluid [Capurro and Barberis, 2014]. Furthermore, the poroelastic Cauchy stress tensor $\boldsymbol{\sigma}^{por}$ can be expressed in terms of the pressure p and the displacement $\boldsymbol{u}$:

$$\boldsymbol{\sigma}^{por}(\boldsymbol{u}, p) \;=\; \boldsymbol{\sigma}(\boldsymbol{u}) \;-\; \alpha p\, \boldsymbol{I}, \tag{2.3}$$

where α is the Biot coefficient, $\boldsymbol{I}$ is the identity tensor, and $\boldsymbol{\sigma}$ is a linear stress tensor. Next, $\boldsymbol{\sigma}$ can be expressed in terms of $\boldsymbol{u}$. This reads

$$\boldsymbol{\sigma}(\boldsymbol{u}) \;=\; 2\mu\boldsymbol{\varepsilon}(\boldsymbol{u}) \;+\; \lambda(\nabla\cdot\boldsymbol{u})\, \boldsymbol{I}, \tag{2.4}$$

where $\boldsymbol{\varepsilon}(\boldsymbol{u}) = \frac{1}{2}(\nabla\boldsymbol{u} + \nabla\boldsymbol{u}^T)$ is the linear strain tensor, and μ and λ are Lamé parameters. The strain tensor describess the deformation of the body of the matrix. This is applicable since we assume that the displacement is much smaller than the relevant dimensions of the body. During the deformation, we assume that the geometry and constitutive properties of the material are unchanged. Further, we combine (2.3)-(2.4):

$$\boldsymbol{\sigma}^{por}(\boldsymbol{u}, p) \;=\; 2\mu\boldsymbol{\varepsilon}(\boldsymbol{u}) \;+\; \lambda\,(\nabla\cdot\boldsymbol{u})\, \boldsymbol{I} \;-\; \alpha p\, \boldsymbol{I}. \tag{2.5}$$

Next, considering the quasi-static formulation, i.e. neglecting the acceleration. The mechanical deformation of a solid-fluid system can then be written as

$$-\nabla\cdot\boldsymbol{\sigma}^{por} = \boldsymbol{f}. \tag{2.6}$$

Here, $\boldsymbol{f}$ is the contribution from body forces in the porous medium. We obtain the first equation of our model by inserting (2.5) in (2.6):

$$-\nabla\cdot[2\mu\boldsymbol{\varepsilon}(\boldsymbol{u}) + \lambda(\nabla\cdot\boldsymbol{u})\boldsymbol{I}] + \alpha\nabla\cdot(p\boldsymbol{I}) = \boldsymbol{f}. \tag{2.7}$$

For the second equation, we consider the mass conservation equation (1.13) derived in Section 1.1.3. We let $\boldsymbol{w} = \rho_f \boldsymbol{w}_v$ and $\Phi_f = \rho_f \phi$ be the mass of the fluid. Then

$$\partial_t \Phi_f = -\nabla \cdot \boldsymbol{w} + \psi. \tag{2.8}$$

Here, Φ_f can be expressed in terms of $\boldsymbol{u}$ and p:

$$\Phi_f(\boldsymbol{u}, p) = \frac{p}{M} + \alpha \nabla \cdot \boldsymbol{u}, \tag{2.9}$$

where M is the Biot modulus. Next, we insert (2.9) in (2.8). This yields

$$\partial_t \left(\frac{p}{M} \; + \; \alpha \, \nabla \cdot \boldsymbol{u} \right) \; + \; \nabla \cdot \boldsymbol{w} \; = \; \psi, \tag{2.10}$$

which is our second equation. The third and last equation is Darcy's law, i.e. (1.10), with $\boldsymbol{w} = \rho_f \boldsymbol{w}_v$:

$$\boldsymbol{w} = -\frac{\boldsymbol{k}\, \rho_f}{\mu_f} \, (\nabla p \; - \; \rho_f \, \boldsymbol{g}).$$

For simplicity, we let $\boldsymbol{K} = \frac{\boldsymbol{k}\rho_f}{\mu_f} = \frac{\boldsymbol{k}}{\nu_f}$, where ν_f is the kinematic viscosity. We rearrange and obtain (2.1c):

$$\boldsymbol{K}^{-1} \boldsymbol{w} + \nabla p \; = \; \rho_f \, \boldsymbol{g}, \tag{2.11}$$

where $\boldsymbol{K}^{-1}$ is the inverse of the permeability tensor divided by ν_f.

2.2 Flow model with lower-dimensional source terms

The aim of this section is to introduce a singularity removal-based technique. [Gjerde et al., 2018] showed that this technique obtained optimal convergence for solving a 3D flow model with 1D Dirac line sources δ_Γ distributed on a 1D line segment $\Gamma \subset \Omega$, i.e. (2.2a)-(2.2b). We let $\Omega \subset \mathbb{R}^3$ be a bounded, open domain with a smooth boundary $\partial\Omega$ and $\Gamma = \cup_{j=1}^m \Gamma_j$ be a collection of m line segments. Then m line sources are defined as:

$$\int_\Omega f \delta_\Gamma \, v \, \mathrm{d}\Omega = \sum_{j=1}^m \int_{\Gamma_j} f(s_j, t) v(s_j) \mathrm{d}S \quad \forall v \in C^0(\bar{\Omega}),$$

where $f(s_j, t) \in H^2(\Gamma_j)$ is the intensity of the line source j, s_j is the arc-length of the line segment j and t is the time.

[Gjerde et al., 2018; Köppl et al., 2016] proved that the lack of convergence was local

to the area surrounding the singularity. Thus, removing a small region R surrounding Γ retrieved optimal convergence for solving (2.2a)-(2.2b). We let $\varepsilon > 0$, then R is given by

$$R = \{(x,y,z) : \sqrt{x^2+y^2} < \varepsilon\}. \tag{2.12}$$

This motivates the need of a singularity removal-based technique. The technique considered was originally found in [Gjerde et al., 2018], but is written for the purpose of verification and convenience for the reader. The technique splits the solution of the pressure into one explicit, low regularity term and one implicit, higher regularity term [Gjerde et al., 2019, 2018]. This reads

$$p = p_s + p_r, \tag{2.13}$$

where p_s captures the singularity and p_r is the high regularity term. To avoid a singular solution, we reformulate (2.2a)-(2.2b) in order to solve for p_r. The actual pressure is obtained by interpolating p_s onto the discrete space of the pressure. Note that the technique introduced in the two sections to come, holds for (A1)-(A2). By (A1), K is independent of the position and the direction of the flow, hence a positive scalar quantity.

For haemodynamics in the brain, we consider the following assumptions:

A1. *Isotropic porous medium.*

A2. *Homogeneous porous medium.*

A3. *Nearly incompressible.*

A4. *Neglecting the gravitational acceleration* $\boldsymbol{g}$.

(A1)-(A4) are usually made when considering flow in the brain, and $\boldsymbol{g}$ is usually neglected in haemodynamics [Formaggia et al., 2009], i.e. dynamics of blood flow.

2.2.1 Illustration of the method

We start by illustrating the singularity removal-based technique for a fixed line source, where we orientated the coordinate system such that Γ is aligned with the z-axis. We further let $f(z,t) \in H^2(\Gamma)$, $\Gamma = (0,0,z) \in \Omega$ be a line segment that passes through the entire domain and (r,θ,z) be cylindrical coordinates with $r = \sqrt{x^2+y^2}$. Then the line singularity term p_s in (2.13) can be expressed as

$$p_s = \frac{f(z,t)G(r)}{K}, \tag{2.14}$$

where the Green's function $G(r) \in L^2(\Omega)$ is given by (1.15). Recall the aim is to reformulate (2.2a)-(2.2b) to obtain a problem which can be solved for the high regularity term p_r. We begin by inserting (2.13) in (2.2a) and then rearrange for convenience:

$$-\nabla \cdot (K\nabla p_r) - \nabla \cdot (K\nabla p_s) = f\delta_\Gamma. \tag{2.15}$$

Further, we find an expression for $-\nabla \cdot (K\nabla p_s)$ by inserting (2.14) in $-\nabla \cdot (K\nabla p_s)$:

$$\begin{aligned} -\nabla \cdot (K\nabla p_s) &= -\nabla \cdot (K\nabla fG) \\ &= -\mathrm{d}_{zz} f\ G - f\Delta G. \end{aligned} \tag{2.16}$$

Next, we substitute the result from (2.16) into (2.15). This yields

$$-\nabla \cdot (K\nabla p_r) - \mathrm{d}_{zz} f\ G - f\Delta G = f\delta_\Gamma. \tag{2.17}$$

The two last terms in (2.17) cancel each other out by the fundamental property (1.16). We rearrange and obtain:

$$-\nabla \cdot (K\nabla p_r) = \mathrm{d}_{zz} f\ G. \tag{2.18}$$

We denote the right-hand side of (2.18) as a function $F \in L^2(\Omega)$. For generalization, we let $F(f) \in L^2(\Omega)$ be a function of the intensity of the Dirac source term. This means that $F(f(z,t))|_{\Gamma=(0,0,z)} = F(f)$. Lastly, we obtain the reformulated boundary conditions by inserting (2.13) in (2.2b). Then the generalized problem with singularity removal reads:

$$-\nabla \cdot (K\nabla p_r) = F \quad \text{in } \Omega, \tag{2.19a}$$

$$p_r = -p_0 + p_{s,0} = p_{r,0} \quad \text{on } \partial\Omega. \tag{2.19b}$$

Remark that

$$F(f(z,t)) = \mathrm{d}_{zz} f(z,t)\ G, \tag{2.20}$$

with G given by (1.15).

2.2.2 Line sources

This chapter is concluded by extending the technique introduced in Section 2.2.1 to consider arbitrary line sources. We let $\Gamma = (r,\theta,z) \subset \Omega$ be an arbitrary line segment between the points $\boldsymbol{a}$ and $\boldsymbol{b}$ for $\boldsymbol{a},\boldsymbol{b} \in \Omega$. We recall the splitting of p, i.e. (2.13) and let p_s be given by

$$p_s = \frac{E(f)G(\boldsymbol{x})}{K}. \tag{2.21}$$

Note that this technique holds for (A1)-(A2). Here, $E(\cdot)$ is an extension operator and $G(\boldsymbol{x}) \in L^2(\Omega)$ satisfies (1.18). We let $E(f) : H^2(\Gamma) \to H^2(\Omega) \cap C^0(\bar{\Omega})$ be the extension of the line source intensity f into the domain Ω. We need to find expressions for both $G(\boldsymbol{x})$ and $E(f)$ in (2.21). This is not as straightforward as for a fixed line source, as illustrated in the previous section. Moreover, we start off by finding $G(\boldsymbol{x})$ since $E(f)$ need to satisfy the reformulated problem given by (2.19a)-(2.19b). Therefore, we first find $G(\boldsymbol{x})$, second $F(E(f))$ and third $E(f)$.

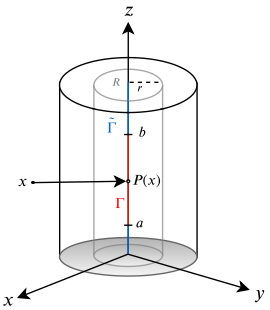

Fig. 2.1 Illustration of a blood vessel with a line segment $\Gamma = \{(0,0,z) : z \in [a,b]\}$ and its elongation $\tilde{\Gamma} = \{(0,0,z) \in \Omega\}$. R is a small region surrounding Γ with radius r. $P : \Omega \to \tilde{\Gamma}$ is a projection operator and projects a point in Ω onto the closest point on $\tilde{\Gamma}$.

An arbitrary line can be expressed as

$$\boldsymbol{y} = \boldsymbol{a} + \boldsymbol{\gamma}\, s \qquad s \in (0, L), \tag{2.22}$$

where $L = \|\boldsymbol{b} - \boldsymbol{a}\|$, s is the arc-length of the line segment, and $\boldsymbol{\gamma} = \frac{\boldsymbol{b}-\boldsymbol{a}}{L}$ is the normalized tangent vector of Γ, which means $\|\boldsymbol{\gamma}\| = 1$. Figure 2.1 illustrates a blood vessel with a 1D line segment going through it. Furthermore, to find the candidate $G(\boldsymbol{x})$, we insert (2.22) in (1.19). This yields

$$G(\boldsymbol{x}) = \frac{1}{4\pi} \int_0^L \frac{1}{\|\boldsymbol{x} - \boldsymbol{a} - \boldsymbol{\gamma} s\|}\, \mathrm{d}\boldsymbol{\gamma}. \tag{2.23}$$

Since $\boldsymbol{\gamma}$ is the normalized, the solution of the integral in (2.23) is

$$G(\boldsymbol{x}) = \frac{1}{4\pi} \ln\left(\frac{\|\boldsymbol{x} - \boldsymbol{b}\| + L + \boldsymbol{\gamma} \cdot (\boldsymbol{a} - \boldsymbol{x})}{\|\boldsymbol{x} - \boldsymbol{a}\| + \boldsymbol{\gamma} \cdot (\boldsymbol{a} - \boldsymbol{x})} \right).$$

We rewrite this solution in its final form to read

$$G(\boldsymbol{x}) = \frac{1}{4\pi} \ln\left(\frac{r_b + L + \boldsymbol{\gamma} \cdot (\boldsymbol{a} - \boldsymbol{x})}{r_a + \boldsymbol{\gamma} \cdot (\boldsymbol{a} - \boldsymbol{x})} \right), \tag{2.24}$$

for

$$r_a := \|\boldsymbol{x} - \boldsymbol{a}\|$$

and

$$r_b := \|\boldsymbol{x} - \boldsymbol{b}\|.$$

Next, we find F, where we use the same approach as in Section 2.2.1. We start by inserting (2.21) in $-\nabla \cdot (K\nabla p_s)$. This gives us

$$\begin{aligned} -\nabla \cdot (K\nabla p_s) &= \Delta[E(f)G] \\ &= G\Delta E(f) + 2\nabla E(f) \cdot \nabla G + E(f)\Delta G. \end{aligned} \tag{2.25}$$

Then we insert the result from (2.25) in (2.17), where we use the fact that $E(f)|_\Gamma = f$:

$$\nabla \cdot (K\nabla p_r) + G\Delta E(f) + 2\nabla E(f) \cdot \nabla G + E(f)\Delta G = -E(f)\delta_\Gamma. \tag{2.26}$$

We observe that by the fundamental property (1.20), the two terms to the right of (2.26) cancel each other out. We then rearrange the remaining part. This reads

$$-\nabla \cdot (K\nabla p_r) = G\Delta E(f) + 2\nabla E(f) \cdot \nabla G. \tag{2.27}$$

We let the right-hand side of (2.27) be $F(E(f))$. That is

$$F(E(f)) = G\Delta E(f) + 2\nabla E(f) \cdot \nabla G. \tag{2.28}$$

Hence, (2.28) satisfies (2.19a)-(2.19b).

Finally, we turn to find an expression for $E(f)$. $E(f)$ needs to be chosen such that $\nabla G_\perp$ is canceled since $\nabla G_\perp$ fails to be integrable in $L^2(\Omega)$ in the neighborhood of Γ. In other words, if we want $p_r \in H^2(\Omega)$ and $F \in L^2(\Omega)$, then $\nabla G_\perp$ needs to be canceled out. The regularity of p_r depends on the choice of $E(f)$. Remark that ∇G can be split into one perpendicular and one parallel part, i.e. $\nabla G = [\nabla G_\perp, \nabla G_\parallel]^T$. We obtain the cancellation of $\nabla G_\perp$ by choosing $E(f)$ such that $\nabla_\perp E(f) = (0,0) \in R$, where R is given by (2.12) and illustrated in Figure 2.1. Further, we assume $f = f(s,t)$ is known, where $f(s,t)$ is a function of the arc-length parameter s and the time t. By these assumptions, a choice of $E(f)$ can be

$$E(f)(\boldsymbol{x},t) = f(P(\boldsymbol{x}),t) \quad \text{for } \boldsymbol{x} \in \Omega, \tag{2.29}$$

where $P : \Omega \to \tilde{\Gamma}$ is a projection operator. We define it as $\boldsymbol{x} \to (\boldsymbol{x} - \boldsymbol{a}) \cdot \boldsymbol{\gamma}$ the orthogonal projection of a point $\boldsymbol{x}$ onto the extension of Γ. The extension of Γ is given by $\tilde{\Gamma} = \{(r, \theta, z) \in \Omega\}$. This is also illustrated in Figure 2.1. Now, we can find a final expression of F. Given the extension (2.29), the terms in (2.28) affected by the gradient and the Laplacian operators are:

$$\nabla G = \frac{1}{4\pi}\left(\frac{\frac{\boldsymbol{x}-\boldsymbol{b}}{r_b} - \boldsymbol{\gamma}}{L + r_a + \boldsymbol{\gamma}\cdot(\boldsymbol{a}-\boldsymbol{x})} - \frac{\frac{\boldsymbol{x}-\boldsymbol{b}}{r_b} - \boldsymbol{\gamma}}{r_a + \boldsymbol{\gamma}\cdot(\boldsymbol{a}-\boldsymbol{x})}\right), \tag{2.30a}$$

$$\nabla E(f) = \mathrm{d}_z f(P(\boldsymbol{x}), t)\boldsymbol{\gamma}, \tag{2.30b}$$

$$\Delta E(f) = \mathrm{d}_{zz} f(P(\boldsymbol{x}), t)\,\|\boldsymbol{\gamma}\| = \mathrm{d}_{zz} f(P(\boldsymbol{x}), t). \tag{2.30c}$$

We now consider $F(f(P(\boldsymbol{x}), t))$ since (2.29). Then the final expression of F is obtained by inserting (2.30a)-(2.30c) in (2.28):

$$F(f(P(\boldsymbol{x}), t)) = \mathrm{d}_{zz} f(P(\boldsymbol{x}), t)G + \mathrm{d}_z f(P(\boldsymbol{x}), t)\frac{1}{2\pi}\left(\frac{1}{r_a} - \frac{1}{r_b}\right), \tag{2.31}$$

where G is given by (2.24).

Chapter 3

Discretization

In this chapter, we will introduce all the mathematical methods used for solving the Biot model with 1D line sources. That is the discretization techniques and iterative schemes. We recall the system of equations:

$$-\nabla\cdot[2\mu\boldsymbol{\varepsilon}(\boldsymbol{u})+\lambda\ (\nabla\cdot\boldsymbol{u})\,\boldsymbol{I}]+\alpha\nabla p=\boldsymbol{f}, \tag{3.1a}$$

$$\partial_t\left(\frac{p}{M}+\alpha\ \nabla\cdot\boldsymbol{u}\right)+\nabla\cdot\boldsymbol{w}=\psi+f\delta_\Gamma, \tag{3.1b}$$

$$\boldsymbol{K}^{-1}\boldsymbol{w}+\nabla p\ =\rho_f\boldsymbol{g}. \tag{3.1c}$$

This mathematical model was introduced in Chapter 2. In (3.1a), we have $\nabla p \notin L^2(\Omega)$ because of the singularity in p. This will be taken care of by partial integration.

The Biot model is usually discretized in time by backward Euler, see e.g. [Both et al., 2017; Mikelić et al., 2014]. Various methods have been developed for spatial-discretization of partial differential equations, e.g. finite differences, finite volumes, and finite elements. Due to its simplicity in analysis, we will consider the finite element method. Even though, our techniques can be used for other discretization methods. We further apply the fixed-stress splitting scheme to decouple the flow and mechanics equations. The fixed-stress splitting scheme is a fast, robust algorithm with good convergence, which is the motivation behind the choice of method.

We will in this chapter introduce a singularity removal-based scheme in order to avoid singular solutions when solving (3.1a)-(3.1c). The scheme combines this splitting technique with the fixed-stress splitting scheme. Let us recall the splitting of the solution of the pressure,

and apply the same splitting technique to $\boldsymbol{w}$. This reads:

$$p = p_s + p_r, \tag{3.2a}$$

$$\boldsymbol{w} = \boldsymbol{w}_s + \boldsymbol{w}_r, \tag{3.2b}$$

where the subscripts s and r indicate the low and high regularity term, respectively. The scheme also employs backward Euler, the finite element method and the fixed-stress splitting scheme. In the last section, we prove optimal convergence for this scheme.

3.1 Finite element method

A method to spatially solve partial differential equations is the Finite Element Method (FEM). The foundation of the FEM is splitting the spatial domain Ω into smaller units or elements, and then approximate the solution on the discretized domain. First, we introduce the conformal variational formulation and then apply it to the mechanics equation (3.1a). Secondly, we introduce the mixed variational formulation, and then apply it to the flow equations (3.1b)-(3.1c). We then introduce the finite element discretization. Here, we introduce the elements used for calculating the pressure, flux and displacement. Lastly, we defined the discrete spaces used to approximate the solutions.

3.1.1 Conformal variational formulation

To explain the conformal variational formulation, we consider the following example:

Example 1 (Poisson equation with Dirichlet boundary conditions)**.** *For some source term S. Find p such that:*

$$-\Delta p \;=\; S \quad \textit{in } \Omega, \tag{3.3a}$$

$$p \;=\; 0 \quad \textit{on } \partial\Omega. \tag{3.3b}$$

Here, (3.3a) *is an elliptic equation, i.e. the information is propagated equally in all directions. To obtain the variational formulation of* (3.3a)-(3.3b)*, we first multiply both sides of the equation with a test function $q \in \tilde{Q}$. We then integrate over the spatial domain. Consequently,* (3.3a)-(3.3b) *becomes:*

$$-\int_\Omega (\Delta p)\, q \, dx = \int_\Omega S\, q \, dx, \tag{3.4}$$

where $p \in Q$ is referred to as the trial function. Next, our intention is to find a weak formulation of (3.4)*. We first use partial integration on the left-hand side of* (3.4)*:*

$$-\int_\Omega (\Delta p)\, q\, dx = \int_\Omega \nabla p \cdot \nabla q\, dx - \int_{\partial\Omega} \frac{\partial p}{\partial \boldsymbol{n}}\, q\, ds, \tag{3.5}$$

where $\boldsymbol{n}$ is a normal vector. The last term of (3.5) *is neglected since q have compact support on Ω. Consequently, we now have a weak form of the problem* (3.3a)*:*
Find $p \in Q$ such that $\forall q \in \hat{Q}$:

$$\int_\Omega \nabla p \cdot \nabla q\, dx = \int_\Omega S\, q\, dx. \tag{3.6}$$

The function spaces $\hat{Q}$ and Q may be different but may also be the same. In the conformal variational formulation, Q and $\hat{Q}$ are the same function space. The function spaces of Q and $\hat{Q}$ depends on the choice of which function space S belongs to. As an example, if we let $S \in L^2(\Omega)$ then Q and $\hat{Q}$ be $H^1(\Omega)$. Furthermore, we observe that the left-hand side of (3.6) *is a function of both p and q. Hence, we can write the left-hand side as the function $a(p,q)$. We also observe that the right-hand side is a function of only q, and can be written as the function $L(q)$. a includes the unknown parts of the equation and L the known parts. This means that we want to solve the linear system $a = L$. For convenience, we rewrite* (3.6) *in terms of the inner product. Then we have the conformal variational formulation of* (3.3a)-(3.3b)*:*

$$\langle \nabla p, \nabla q \rangle = \langle S, q \rangle.$$

We apply the same approach as in Example 1 to the mechanics equation (3.1a). Let $\boldsymbol{f} \in L^2(\Omega)$. Then the conformal variational formulation problem reads:

Problem 1. *Let $p \in L^2(\Omega)$ be given, then find $\boldsymbol{u} \in H^1(\Omega)$ such that $\forall \boldsymbol{v} \in H^1(\Omega)$:*

$$\langle 2\mu\boldsymbol{\varepsilon}(\boldsymbol{u}), \boldsymbol{\varepsilon}(\boldsymbol{v}) \rangle + \langle \lambda \nabla \cdot \boldsymbol{u}, \nabla \cdot \boldsymbol{v} \rangle - \langle \alpha p, \nabla \cdot \boldsymbol{v} \rangle = \langle \boldsymbol{f}, \boldsymbol{v} \rangle. \tag{3.7}$$

3.1.2 Mixed variational formulation

The mixed finite element method differentiates from the conformal by having the property of local mass conservation [Matthies and Tobiska, 2007]. This is also a motivation behind

the choice of method. Mass conservation is a useful property in the biomedical field, e.g. studying the blood flow of drug delivery through microcirculation [Cattaneo and Zunino, 2014; Possenti et al., 2018] and the efficiency of cancer treatment by hypothermia [Nabil and Zunino, 2016]. In a mixed finite element problem, we consider more than one finite element at once and the choice of both elements and function spaces determine whether the scheme is stable. A naive choice of combination of elements can lead to a unstable scheme. The flow equations (3.1b)-(3.1c) are solved with this method. Therefore, we will now introduce the mixed variational formulation.

We consider the following example to explain the mixed variational formulation:

Example 2 (Mixed problem with Dirichlet boundary condition)**.** *Let $S \in L^2(\Omega)$ be a source term. Then we consider the strong formulation of the following problem:*
Find $(\boldsymbol{w}, p)$ such that:

$$\nabla \cdot \boldsymbol{w} = S \quad \text{in } \Omega, \tag{3.8a}$$

$$\boldsymbol{K}^{-1}\boldsymbol{w} + \nabla p = 0 \quad \text{in } \Omega, \tag{3.8b}$$

$$p \;=\; p_0 \quad \text{on } \partial\Omega. \tag{3.8c}$$

We let W and $\hat{W}$ be mixed function spaces. Then, by the same approach as in Example 1, a weak formulation of (3.8a)-(3.8c) *in terms of the inner product reads:*
Find $(\boldsymbol{w}, p) \in W$ such that $\forall (\boldsymbol{z}, q) \in \hat{W}$:

$$\langle \boldsymbol{K}^{-1}\boldsymbol{w}, \boldsymbol{z}\rangle \; - \langle p, \nabla \cdot \boldsymbol{z}\rangle \; + \langle p_0\, \boldsymbol{z},\, \boldsymbol{n}\rangle_{\partial\Omega} \; = 0 \qquad \forall \boldsymbol{w}, \boldsymbol{z} \in H(div;\Omega),$$

$$\langle \nabla \cdot \boldsymbol{w}, q\rangle \;=\; \langle S, q\rangle \qquad\qquad \forall p, q \in L^2(\Omega).$$

Here, $\langle p_0\, \boldsymbol{z}_h,\, \boldsymbol{n}\rangle_{\partial\Omega}$ are the boundary conditions. In a mixed problem, the Dirichlet boundary conditions are Neumann boundary conditions. As in Example 1, W and $\hat{W}$ may be different but also the same function space. A natural choice of function spaces for this mixed problem is $W = \hat{W} = H(div;\Omega) \times L^2(\Omega)$.

Now, we apply the mixed variational formulation to (3.1b)-(3.1c) as shown in Example 2. We let $\psi \in L^2(\Omega)$, $\rho_f \in \mathbb{R}$, $\boldsymbol{g} \in \mathbb{R}^d$ for $d \in \{2, 3\}$ and $\delta_\Gamma \notin L^2(\Omega)$. Then the problem reads:

Problem 2. *Given $\boldsymbol{u} \in H^1(\Omega)$. Find $(p, \boldsymbol{w}) \in L^2(\Omega) \times H(div;\Omega)$ such that $\forall (q, \boldsymbol{z}) \in L^2(\Omega) \times H(div;\Omega)$:*

$$\left\langle \frac{1}{M}\partial_t p, q \right\rangle + \langle \alpha \partial_t (\nabla \cdot \boldsymbol{u}), q\rangle + \langle \nabla \cdot \boldsymbol{w}, q\rangle = \langle \psi, q\rangle + \langle f, q\rangle_\Gamma, \tag{3.10a}$$

$$\langle \boldsymbol{K}^{-1}\boldsymbol{w},\boldsymbol{z}\rangle - \langle p,\nabla\cdot\boldsymbol{z}\rangle = \langle \rho_f \boldsymbol{g},\boldsymbol{z}\rangle. \tag{3.10b}$$

We have now introduced the conformal and mixed variational formulation and applied them to (3.1a) and (3.1b)-(3.1c), respectively. Before defining the discrete spaces, we will introduce finite element discretization. Here, we introduce our choice of elements and expected order of convergence for a problem with these elements.

3.1.3 Finite element discretization

In the FEM, as previously stated, the spatial domain is discretized into smaller units or elements in order to approximate the solution. In two dimensions, the elements are usually triangles and in three dimensions tetrahedrons, but they may be other types of elements. We let $\mathscr{T}_h$ be the mesh of $\bar{\Omega}$, where the subscript h denotes the variable spatially discretized by mesh size h. The mesh is a collection of the elements, and can be expressed as a set of these elements. Let us consider triangle elements denoted as t. Then $\mathscr{T}_h$ is a set of triangles $\{\mathrm{t}\}$ such that

$$\bar{\Omega} = \bigcup_{\mathrm{t}\in\mathscr{T}_h} \mathrm{t}.$$

We discretize (3.1a)-(3.1c) in space by $\mathbb{P}_1$, $\mathbb{P}_0$, and $\mathbb{RT}_0$ elements to approximate the displacement, the pressure, and the flux, respectively. $\mathbb{P}_1$ elements are linear piecewise polynomials. We consider the Continuous Lagrange elements denoted as $\mathbb{CG}_1$. These elements have one nodal value on each edge of the element. $\mathbb{CG}_1$ as a triangle element is illustrated in Figure 3.1(a). Further, $\mathbb{P}_0$ elements are piecewise constants. Here, we consider Discontinuous Lagrange elements, which are denoted as $\mathbb{DG}_0$. These elements only have one nodal value in the center of the element. This is illustrated for a triangle element in Figure 3.1(b). Lastly, we consider a vector space of $\mathbb{R}^d$-valued polynomials given by $\mathbb{RT}_0 = \boldsymbol{a}_1 + b_1\boldsymbol{x}$, where $\boldsymbol{a}_1 \in \mathbb{R}^d$ and $b_1 \in \mathbb{R}$. These elements have a normal component on each corner of the triangle. $\mathbb{RT}_0$ as a triangle element is illustrated in Figure 3.1(c).

The expected order of convergence for the solutions when using the FEM depends on the choice of elements and the regularity of the solution. Solving (3.7) by FEM with $\mathbb{P}_1$ elements for the displacement, i.e. the conformal FEM, yields optimal $\mathscr{O}(h^2)$ of convergence in the $L^2(\Omega)$-norm and $\mathscr{O}(h^1)$ in the $H^1(\Omega)$-norm. Furthermore, solving (3.10a)-(3.10b) when $f = 0$ by the mixed FEM with $\mathbb{P}_0 - \mathbb{RT}_0$ elements for pressure and flux, respectively, the optimal convergence is $\mathscr{O}(h^1)$ in the $L^2(\Omega)$-norm.

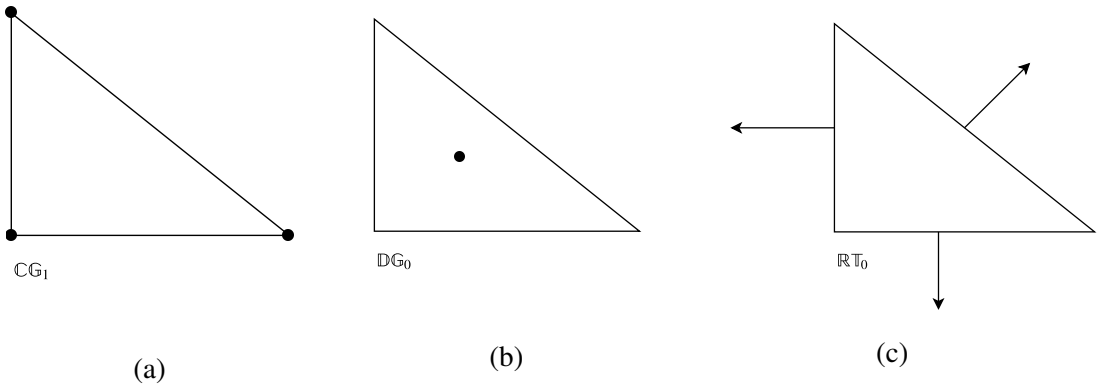

(a) (b) (c)

Fig. 3.1 Illustration of the triangle elements: Continuous Lagrange ($\mathbb{CG}_1$) (a), Discontinuous Lagrange ($\mathbb{DG}_0$) (b), and Raviart-Thomas ($\mathbb{RT}_0$) (c). The black dots and arrows indicate the degrees of freedom of the element. The subscripts denote the order of polynomials.

3.1.4 Discrete spaces

In the last section of FEM, we define the discrete spaces. They are written as in [Both et al., 2017]. We let $\Omega \subset \mathbb{R}^d$ where $d \in \{2,3\}$, then the discrete spaces read

$$\boldsymbol{V}_h = \{\, \boldsymbol{v}_h \in [\, H_0^1(\Omega)\,]^d \mid \forall \mathfrak{t} \in \mathscr{T}_h,\, \boldsymbol{v}_{h|\,\mathfrak{t}} \in [\,\mathbb{P}_1\,]^d \},$$

$$Q_h = \{\, q_h \in L^2(\Omega) \mid \forall \mathfrak{t} \in \mathscr{T}_h,\, q_{h|\mathfrak{t}} \in \mathbb{P}_0 \},$$

$$\boldsymbol{Z}_h = \{ \boldsymbol{z}_h \in H(div;\Omega) \mid \forall \mathfrak{t} \in \mathscr{T}_h,\, \boldsymbol{z}_{h|\mathfrak{t}}(\boldsymbol{x}) = \boldsymbol{a}_1 + b_1 \boldsymbol{x},\, \boldsymbol{a}_1 \in \mathbb{R}^d, b_1 \in \mathbb{R} \}.$$

3.2 Iterative solver for Biot's equations

In the previous section, we introduced the finite element method and used it to spatially discretize (3.1a)-(3.1c). We now turn to discretize (3.1a)-(3.1c) in the time, and introducing the iterative scheme and a singularity removal-based scheme. There are two alternatives to solve the fully coupled Biot model; monolithically or with an iterative splitting method. We consider the widely used fixed-stress splitting scheme, see e.g. [Bause et al., 2016; Borregales et al., 2018; Storvik et al., 2018]. This is motivated by the fact that it is unconditionally stable and easier to implement. Here, a stabilization term is added to the flow equation (adding it to mechanics equation is the undrained splitting scheme).

For the purpose of solving (3.1a)-(3.1c) without singular solutions, our approach is to develop a singularity removal-based scheme. We recall as previously mentioned that the scheme employs the splitting of the solutions of the pressure and the flux [Gjerde et al.,

2018], i.e. (3.2a)-(3.2b), and the fixed-stress splitting scheme.

For $d \in \{2,3\}$, the standard assumptions for these schemes, see e.g. [Both et al., 2017], read:

A5. *Let $\rho_f \in \mathbb{R}$, $\boldsymbol{g} \in \mathbb{R}^d$ be constant.*

A6. *Let $M, \alpha, \mu, \lambda \in L^\infty(\Omega)$ be positive, uniformly bounded, with the lower bounded strictly positive.*

A7. *Let $\boldsymbol{K} \in L^\infty(\Omega)^{d\times d}$ be a symmetric matrix, which is constant in time and has uniformly bounded eigenvalues, i.e., there exist constants $k_m, k_M \in \mathbb{R}$, satisfying for all $\boldsymbol{x} \in \Omega$ and for all $\boldsymbol{z} \in \mathbb{R}^d \backslash \{0\}$ i.e. not zero.*

$$0 < k_m \, \boldsymbol{z}^T \boldsymbol{z} \leq \boldsymbol{z}^T \boldsymbol{K}(x) \, \boldsymbol{z} \leq k_M \, \boldsymbol{z}^T \boldsymbol{z} < \infty$$

3.2.1 Backward Euler

The Biot model is usually discretized in time by the backward Euler, see e.g. [Both et al., 2017; Mikelić et al., 2014]. The method has the form

$$y^n = y^{n-1} + \tau \, u(t^n, y^n),$$

where the superscript n indicates the current time level and $n-1$ the previous time level. $\tau := \frac{T}{N}$ is the time step and $t^n := n\tau$ for $n \in \mathbb{N}$. Here, T and N are the final time and the total number of time steps, respectively. Moreover, this is an implicit method, and its main advantage is the unconditional stability. Though, it is more costly to implement than an explicit method. However, an explicit method is not unconditionally stable. Furthermore, backward Euler is a one-step method since $\forall n \geq 0$ only depends on y^n [Quarteroni et al., 2007].

We will now apply backward Euler to Problem 1-2, i.e. (3.7), (3.10a) and (3.10b). We include the subscript h for the spatial-discretization. Further, we let $(\boldsymbol{u}_h^0, p_h^0, \boldsymbol{w}_h^0) \in \boldsymbol{V}_h \times Q_h \times \boldsymbol{Z}_h$ be the initial values. Note that the discrete spaces defined in Section 3.1.4. Further, we let the solution of the displacement, the pressure, and the flux for the previous time time step be known. Then we have: Given $(\boldsymbol{u}_h^{n-1}, p_h^{n-1}, \boldsymbol{w}_h^{n-1}) \in \boldsymbol{V}_h \times Q_h \times \boldsymbol{Z}_h$. Find $(\boldsymbol{u}_h^n, p_h^n, \boldsymbol{w}_h^n) \in \boldsymbol{V}_h \times Q_h \times \boldsymbol{Z}_h$:

$$\langle 2\mu \boldsymbol{\varepsilon}(\boldsymbol{u}_h^n), \boldsymbol{\varepsilon}(\boldsymbol{v}_h)\rangle + \langle \lambda(\nabla \cdot \boldsymbol{u}_h^n), \nabla \cdot \boldsymbol{v}_h\rangle - \langle \alpha p_h^n, \nabla \cdot \boldsymbol{v}_h\rangle = \langle \boldsymbol{f}^n, \boldsymbol{v}_h\rangle, \tag{3.11a}$$

$$\left\langle \frac{1}{M} p_h^n, q_h \right\rangle + \langle \alpha \nabla \cdot \boldsymbol{u}_h^n, q_h \rangle + \tau \langle \nabla \cdot \boldsymbol{w}_h^n, q_h \rangle = \tau \langle \psi^n, q_h \rangle + \tau \langle f^n, q_h \rangle_\Gamma + \left\langle \frac{1}{M} p_h^{n-1}, q_h \right\rangle + \langle \alpha \nabla \cdot \boldsymbol{u}_h^{n-1}, q_h \rangle, \tag{3.11b}$$

$$\langle \boldsymbol{K}^{-1} \boldsymbol{w}_h^n, \boldsymbol{z}_h \rangle - \langle p_h^n, \nabla \cdot \boldsymbol{z}_h \rangle = \langle \rho_f \boldsymbol{g}, \boldsymbol{z}_h \rangle, \tag{3.11c}$$

for all $(\boldsymbol{v}_h, q_h, \boldsymbol{z}_h) \in \boldsymbol{V}_h \times Q_h \times \boldsymbol{Z}_h$. We now turn to introduce the fixed-stress splitting scheme, and then apply it to (3.11a)-(3.11c).

3.2.2 Fixed-stress splitting scheme

The fixed-stress splitting scheme is a popular iterative splitting scheme for solving the fully coupled Biot model, see e.g. [Almani et al., 2016]. [Both et al., 2017; Mikelić et al., 2014] proved global, linear convergence for this scheme. It has been widely used for finding the solution to coupled flow and mechanics problems [Gaspar and Rodrigo, 2017]. The scheme has a 'fixed' stress, and the idea is that an artificial volumetric stress $\sigma_\beta = \sigma_0 + K_{dr} \nabla \cdot \boldsymbol{u} - \alpha p$ is kept constant. $K_{dr} \in L^\infty(\Omega)$ is referred to as the drained bulk modulus. In this scheme, we will consider the tuning parameter $\beta_{FS} = \alpha^2 / K_{dr}$. The theoretically optimal choice of β_{FS} is shown in [Both et al., 2017]. The optimal β_{FS} is the same for the fixed-stress splitting scheme with singularity removal, which will be introduced in Section 3.2.3. Hence, β_{FS} is also shown in the proof of convergence in Section 3.3.

We now apply the fixed-stress splitting scheme to (3.11a)-(3.11c). First, we define a sequence $(\boldsymbol{u}_h^{n,i},\ p_h^{n,i},\ \boldsymbol{w}_h^{n,i})$, $i \geq 0$. Let i denote the current iteration step and $i-1$ denote the previous iteration step. We initialize $\boldsymbol{u}$, p and $\boldsymbol{w}$ by $\boldsymbol{u}_h^{n,0} = \boldsymbol{u}_h^{n-1}$, $p_h^{n,0} = p_h^{n-1}$ and $\boldsymbol{w}_h^{n,0} = \boldsymbol{w}_h^{n-1}$, respectively. The scheme iterates until a stopping criterion is reached. The full scheme reads:
Step 1: Given $(\boldsymbol{u}_h^{n,i-1},\ p_h^{n,i-1},\ \boldsymbol{w}_h^{n,i-1}) \in \boldsymbol{V}_h \times Q_h \times \boldsymbol{Z}_h$. Find $(p_h^{n,i},\ \boldsymbol{w}_h^{n,i}) \in Q_h \times \boldsymbol{Z}_h$ such that $\forall (q_h,\ \boldsymbol{z}_h) \in Q_h \times \boldsymbol{Z}_h$:

$$\left\langle \left(\frac{1}{M} + \beta_{FS} \right) p_h^{n,i}, q_h \right\rangle + \tau \langle \nabla \cdot \boldsymbol{w}_h^{n,i}, q_h \rangle = \tau \langle \psi^n, q_h \rangle + \tau \langle f^n, q_h \rangle_\Gamma + \left\langle \frac{1}{M} p_h^{n-1}, q_h \right\rangle + \langle \alpha \nabla \cdot \boldsymbol{u}_h^{n-1}, q_h \rangle + \langle \beta_{FS}\ p_h^{n,i-1}, q_h \rangle - \langle \alpha \nabla \cdot \boldsymbol{u}_h^{n,i-1}, q_h \rangle, \tag{3.12a}$$

$$\langle \boldsymbol{K}^{-1} \boldsymbol{w}_h^{n,i}, \boldsymbol{z}_h \rangle - \langle p_h^{n,i}, \nabla \cdot \boldsymbol{z}_h \rangle = \langle \rho_f \boldsymbol{g}, \boldsymbol{z}_h \rangle. \tag{3.12b}$$

Step 2: Given $p_h^{n,i} \in Q_h$. Find $\boldsymbol{u}_h^{n,i} \in \boldsymbol{V}_h$, such that $\forall \boldsymbol{v}_h \in \boldsymbol{V}_h$:

$$\langle 2\mu\boldsymbol{\varepsilon}(\boldsymbol{u}_h^{n,i}), \boldsymbol{\varepsilon}(\boldsymbol{v}_h)\rangle + \langle \lambda(\nabla\cdot\boldsymbol{u}_h^{n,i}), \nabla\cdot\boldsymbol{v}_h\rangle = \langle \alpha p_h^{n,i}, \nabla\cdot\boldsymbol{v}_h\rangle + \langle \boldsymbol{f}^n, \boldsymbol{v}_h\rangle. \tag{3.12c}$$

We let $(\boldsymbol{p}_h^i, \boldsymbol{w}_h^i, \boldsymbol{u}_h^i)$ denote the solutions at iteration step i and $(\boldsymbol{p}_h^{i-1}, \boldsymbol{w}_h^{i-1}, \boldsymbol{u}_h^{i-1})$ denote the solutions at the previous iteration step $i-1$. Then for $\varepsilon_a, \varepsilon_r > 0$, the stopping criterion is given by

$$\left\|(\boldsymbol{p}_h^i, \boldsymbol{w}_h^i, \boldsymbol{u}_h^i) - (\boldsymbol{p}_h^{i-1}, \boldsymbol{w}_h^{i-1}, \boldsymbol{u}_h^{i-1})\right\| \leq \varepsilon_a + \varepsilon_r \left\|(\boldsymbol{p}_h^i, \boldsymbol{w}_h^i, \boldsymbol{u}_h^i)\right\|. \tag{3.13}$$

In addition, ε_a and ε_r are the absolute and relative error tolerances, respectively.

3.2.3 Fixed-stress splitting scheme with singularity removal

Finally, we introduce a singularity removal-based scheme. Our goal is to introduce a scheme that avoids singular solutions when solving (3.1a)-(3.1c). The scheme is based on splitting the solutions of p and $\boldsymbol{w}$ into one low (explicit) regularity term and one high (implicit) regularity term denoted by the subscript s and r [Gjerde et al., 2019], respectively. In contrast to the standard formulation of the fixed-stress splitting scheme, this scheme is solved by three steps. The first step solves (3.1b)-(3.1c) to get p_r and $\boldsymbol{w}_r$ using (3.2a)-(3.2b). Secondly, p and $\boldsymbol{w}$ are reconstructed by interpolating p_s and $\boldsymbol{w}_s$ onto the discrete spaces of p and $\boldsymbol{w}$, respectively. Third, solving (3.1a) to get $\boldsymbol{u}$.

We start off by reformulating (3.1b)-(3.1c) in order to solve for p_r and $\boldsymbol{w}_r$. Next, we discretize the system of equations by using backward Euler in time and the finite element method in space. Lastly, we apply the fixed-stress splitting scheme. This scheme holds for (A2) and (A5)-(A7). We let $f \in H^2$ and recall the flow model with singular removal introduced in Section 2.2. It is given by (2.19a)-(2.19b), where (2.19b) is the Dirichlet boundary conditions. We will first reformulate (3.1c) and then (3.1b).

To begin, we insert (3.2a)-(3.2b) in (3.1c). Then

$$\boldsymbol{w}_s + \boldsymbol{w}_r = -\boldsymbol{K}\nabla(p_s + p_r - \rho_f \boldsymbol{g}).$$

We have the relation $\boldsymbol{w}_s = -\boldsymbol{K}\nabla p_s$. Rearranging to obtain Darcy's law with singularity removal:

$$\boldsymbol{K}^{-1}\boldsymbol{w}_r + \nabla p_r = \rho_f \boldsymbol{g}. \tag{3.14}$$

According to (3.14), we have

$$-\nabla \cdot (\boldsymbol{K} \nabla p_r) = \nabla \cdot \boldsymbol{w}_r.$$

As a result, (2.19a) becomes

$$\nabla \cdot \boldsymbol{w}_r = F(f). \tag{3.15}$$

Providing that (A1) holds, then for a line segment going through the entire domain F is given by (2.20) and for an arbitrary line segment F is given by (2.20) and (2.31), respectively. Moreover, we next obtain the flow equation with singularity removal by inserting (3.2a), (3.2b) and (3.15) into (3.1b). This reads

$$\partial_t \left(\frac{(p_s + p_r)}{M} \; + \; \alpha \, \nabla \cdot \boldsymbol{u} \right) \; + \; \nabla \cdot \boldsymbol{w}_r \; = \; \psi + F(f),$$

where ψ is the source term solving the time-derivative term in (3.1b). After rearranging, we obtain

$$\partial_t \left(\frac{p_r}{M} \; + \; \alpha \, \nabla \cdot \boldsymbol{u} \right) \; + \; \nabla \cdot \boldsymbol{w}_r \; = \psi_{sr}. \tag{3.16}$$

Here, the source term with singularity removal is given by

$$\psi_{sr} = \psi + F(f) - \frac{\partial_t p_s}{M}.$$

We now apply the finite element method as the spatial-discretization and backward Euler as the time-discretization. Then we obtain the weak formulation of (3.1a), (3.14) and (3.16). In addition, we include the spatial- and time-discretization of (3.2a)-(3.2b). Accordingly, we have

$$\langle 2\mu \boldsymbol{\varepsilon}(\boldsymbol{u}_h^n), \boldsymbol{\varepsilon}(\boldsymbol{v}_h) \rangle + \langle \lambda (\nabla \cdot \boldsymbol{u}_h^n), \nabla \cdot \boldsymbol{v}_h \rangle - \langle \alpha p_h^n, \nabla \cdot \boldsymbol{v}_h \rangle = \langle \boldsymbol{f}^n, \boldsymbol{v}_h \rangle, \tag{3.17a}$$

$$\begin{aligned} \langle \frac{1}{M} p_{r,h}^n, q_h \rangle + \langle \alpha \nabla \cdot \boldsymbol{u}_h^n, q_h \rangle + \tau \langle \nabla \cdot \boldsymbol{w}_{r,h}^n, q_h \rangle &= \tau \langle \psi_{sr}^n, q_h \rangle \\ &+ \langle \frac{1}{M} p_{r,h}^{n-1}, q_h \rangle \\ &+ \langle \alpha \nabla \cdot \boldsymbol{u}_h^{n-1}, q_h \rangle, \end{aligned} \tag{3.17b}$$

$$\langle \boldsymbol{K}^{-1} \boldsymbol{w}_{r,h}^n, \boldsymbol{z}_h \rangle + \langle p_{r,h}^n, \nabla \cdot \boldsymbol{z}_h \rangle = \langle \rho_f \boldsymbol{g}, \boldsymbol{z}_h \rangle, \tag{3.17c}$$

$$p_h^n = p_{s,h}^n + p_{r,h}^n, \tag{3.17d}$$

$$\boldsymbol{w}_h^n = \boldsymbol{w}_{s,h}^n + \boldsymbol{w}_{r,h}^n. \tag{3.17e}$$

Finally, we interpret the fixed-stress splitting scheme. This scheme has one additional step in comparison with the standard schemes. Recalling that the theoretically optimal β_{FS} is shown in the proof of convergence in Section 3.3. Furthermore, we start by initializing $\boldsymbol{u}$, p_r and $\boldsymbol{w}_r$ by $\boldsymbol{u}_h^{n,0} = \boldsymbol{u}_h^{n-1}$, $p_{r,h}^{n,0} = p_{r,h}^{n-1}$ and $\boldsymbol{w}_{r,h}^{n,0} = \boldsymbol{w}_{r,h}^{n-1}$, respectively. Then the full scheme for (3.17a)-(3.17e) reads:

Step 1: Given $(\boldsymbol{u}_h^{n,i-1},\ p_{r,h}^{n,i-1},\ \boldsymbol{w}_{r,h}^{n,i-1}) \in \boldsymbol{V}_h \times Q_h \times \boldsymbol{Z}_h$. Find $(p_{r,h}^{n,i},\ \boldsymbol{w}_{r,h}^{n,i}) \in Q_h \times \boldsymbol{Z}_h$ such that $\forall (q_h,\ \boldsymbol{z}_h) \in Q_h \times \boldsymbol{Z}_h$:

$$\begin{aligned}\left\langle \left(\frac{1}{M} + \beta_{FS}\right) p_{r,h}^{n,i}, q_h \right\rangle + \tau \langle \nabla \cdot \boldsymbol{w}_{r,h}^{n,i}, q_h \rangle = \tau \langle \psi_{sr}^n, q_h \rangle \\ + \left\langle \frac{1}{M}\, p_{r,h}^{n-1}, q_h \right\rangle \\ + \langle \alpha \nabla \cdot \boldsymbol{u}_h^{n-1}, q_h \rangle \\ + \langle\, \beta_{FS}\, p_{r,h}^{n,i-1}, q_h \rangle \\ - \langle \alpha \nabla \cdot \boldsymbol{u}_h^{n,i-1}, q_h \rangle,\end{aligned} \tag{3.18a}$$

$$\langle \boldsymbol{K}^{-1} \boldsymbol{w}_{r,h}^{n,i}, \boldsymbol{z}_h \rangle - \langle p_{r,h}^{n,i}, \nabla \cdot \boldsymbol{z}_h \rangle = \langle \rho_f \boldsymbol{g}, \boldsymbol{z}_h \rangle. \tag{3.18b}$$

Step 2: Given $(p_{r,h}^{n,i}, p_{s,h}^n, \boldsymbol{w}_{r,h}^{n,i}, \boldsymbol{w}_{s,h}^n) \in Q_h \times Q_h \times \boldsymbol{Z}_h \times \boldsymbol{Z}_h$. Find $(p_h^{n,i}, \boldsymbol{w}_h^{n,i}) \in Q_h \times \boldsymbol{Z}_h$:

$$p_h^{n,i} = p_{s,h}^n + p_{r,h}^{n,i}, \tag{3.18c}$$

$$\boldsymbol{w}_h^{n,i} = \boldsymbol{w}_{s,h}^n + \boldsymbol{w}_{r,h}^{n,i}. \tag{3.18d}$$

Step 3: Given $p_h^{n,i} \in Q_h$. Find $\boldsymbol{u}_h^{n,i} \in \boldsymbol{V}_h$ such that $\forall \boldsymbol{v}_h \in \boldsymbol{V}_h$:

$$\langle 2\mu \boldsymbol{\varepsilon}(\boldsymbol{u}_h^{n,i}), \boldsymbol{\varepsilon}(\boldsymbol{v}_h) \rangle + \langle \lambda (\nabla \cdot \boldsymbol{u}_h^{n,i}), \nabla \cdot \boldsymbol{v}_h \rangle = \langle \alpha p_h^{n,i}, \nabla \cdot \boldsymbol{v}_h \rangle + \langle \boldsymbol{f}^n, \boldsymbol{v}_h \rangle. \tag{3.18e}$$

The stopping criterion becomes

$$\left\| (\boldsymbol{p}_{r,h}^i,\ \boldsymbol{w}_{r,h}^i,\ \boldsymbol{u}_h^i) - (\boldsymbol{p}_{r,h}^{i-1},\ \boldsymbol{w}_{r,h}^{i-1},\ \boldsymbol{u}_h^{i-1}) \right\| \ \leq\ \varepsilon_a + \varepsilon_r \left\| (\boldsymbol{p}_{r,h}^i,\ \boldsymbol{w}_{r,h}^i,\ \boldsymbol{u}_h^i) \right\|. \tag{3.19}$$

We call (3.18a)-(3.18e) the fixed-stress splitting scheme with singularity removal.

3.3 Convergence analysis

We conclude this chapter by proving convergence for the fixed-stress splitting scheme with singularity removal for homogeneous porous media. The scheme is given by (3.18a)-(3.18e).

We will also consider the time-discretized equations (3.17a)-(3.17e). The proof is included for the sake of completeness, even though it is only a special case of the proof in [Both et al., 2017]. Hence, the foregoing scheme extends easily to include heterogeneous media. Theorem 7 is extended by (3.24)-(3.25) in comparison to the theorem in [Both et al., 2017]. The proof is also more detailed. Moreover, Lemma 1-5 are the primary technical tools in the proof. It holds for $d \in \{2,3\}$, and (A2) and (A5)-(A7). Additionally, we use the Banach contraction argument, proving that the method is a fixed-point contraction.

We begin by showing an inequality which will be used later in the proof. The definition of the strain tensor reads:

$$\begin{aligned}\|\boldsymbol{\varepsilon}(\boldsymbol{u})\|^2 &= \int_\Omega \sum_{i,j}^{d} \left(\frac{\partial \varepsilon_{i,j}}{\partial x_i}\right)^2 \mathrm{d}\boldsymbol{x} \\ &= \int_\Omega \left(\sum_{i}^{d} \left(\frac{\partial u_i}{\partial x_i}\right)^2 + \sum_{\substack{i\neq j \\ i,j=1}}^{d} \left(\frac{\partial u_i}{\partial x_j} + \frac{\partial u_j}{\partial x_i}\right)^2 \right) \mathrm{d}\boldsymbol{x}.\end{aligned}$$

After applying the AM-RMS inequality (Lemma 5), we achieve the desired inequality:

$$\|\boldsymbol{\varepsilon}(\boldsymbol{u})\|^2 \geq d \int_\Omega \sum_{i=1}^{d} \left(\frac{\partial u_i}{\partial x_i}\right)^2 \mathrm{d}\boldsymbol{x} = d \left\|\nabla \cdot u_h\right\|^2. \tag{3.20}$$

Theorem 7 (Linear convergence for fixed-stress splitting scheme with singularity removal)**.** *Assume* (A2) *and* (A5)-(A7)*. Let* $(\boldsymbol{u}_h^n,\ p_{r,h}^n,\ \boldsymbol{w}_{r,h}^n,\ p_h^n, \boldsymbol{w}_h^n)$ *and* $(\boldsymbol{u}_h^{n,i},\ p_{r,h}^{n,i},\ \boldsymbol{w}_{r,h}^{n,i},\ p_h^{n,i}, \boldsymbol{w}_h^{n,i})$ *be solutions of* (3.17a)-(3.17e) *and* (3.18a)-(3.18e)*, respectively. Let* $e_{p_r}^i = p_{r,h}^{n,i} - p_{r,h}^n$, $e_{\boldsymbol{w}_r}^i = \boldsymbol{w}_{r,h}^{n,i} - \boldsymbol{w}_{r,h}^n$, $e_{\boldsymbol{u}}^i = \boldsymbol{u}_h^{n,i} - \boldsymbol{u}_h^n$, $e_p^i = p_h^{n,i} - p_h^n$ *and* $e_{\boldsymbol{w}}^i = \boldsymbol{w}_h^{n,i} - \boldsymbol{w}_h^n$ *denote the errors at the current iteration. Then for all*

$$\beta_{FS} \ \geq \ \frac{\alpha^2}{2(\frac{2}{d}\mu + \lambda)} \tag{3.21}$$

it holds

$$\left\|e_{p_r}^i\right\|^2 \leq \frac{\frac{\beta_{FS}}{2}}{\frac{1}{M} + \frac{\beta_{FS}}{2} + \frac{\tau k_m}{C_{\Omega,d}}} \left\|e_{p_r}^{i-1}\right\|^2 \tag{3.22}$$

and

$$2\mu \left\|\boldsymbol{\varepsilon}(e_{\boldsymbol{u}}^i)\right\|^2 + \lambda \left\|\nabla \cdot e_{\boldsymbol{u}}^i\right\|^2 \leq \frac{\alpha^2}{\frac{2}{d}\mu + \lambda} \left\|e_p^i\right\|^2 \tag{3.23}$$

where

$$e_p = e_{p_r}, \tag{3.24}$$

and

$$e_{\boldsymbol{w}} = e_{\boldsymbol{w}_r}. \tag{3.25}$$

Optimal convergence rates are obtained when equality holds in (3.21)*.*

Remark. *Under the assumptions stated in Theorem 7,* (3.22) *is a contraction. Therefore, as* $i \to \infty$ *the error of the pressure goes to zero geometrically, and with* (3.23) *for in hand, it implies that error in the difference in iterations of the displacement term goes to zero.*

Proof. **Step 1: Flow with singularity removal and mechanics**
First, we subtract (3.18a) from (3.17b), and (3.18e) from (3.17a). Second, we add the two equations together. Here, we test $\boldsymbol{v}_h = e_{\boldsymbol{u}}^{i-1} \in \boldsymbol{V}_h$, $q_h = e_{p_r}^{i-1} \in Q_h$ and $\boldsymbol{z}_h = \tau e_{\boldsymbol{w}_r}^{i-1} \in \boldsymbol{Z}_h$. This yields

$$\frac{1}{M}\left\|e_{p_r}^i\right\|^2 + \beta_{FS}\langle e_{p_r}^i - e_{p_r}^{i-1}, e_{p_r}^i\rangle + \tau\langle \boldsymbol{K}^{-1} e_{\boldsymbol{w}_r}^i, e_{\boldsymbol{w}_r}^i\rangle + 2\mu\langle \boldsymbol{\varepsilon}(e_{\boldsymbol{u}}^i), \boldsymbol{\varepsilon}(e_{\boldsymbol{u}}^{i-1})\rangle + \lambda\langle \nabla\cdot e_{\boldsymbol{u}}^i, \nabla\cdot e_{\boldsymbol{u}}^{i-1}\rangle = 0.$$

Further, we apply the Polarization (Lemma 1) and Binomial identity (Lemma 2). After rearranging, we have

$$\begin{aligned} \frac{\mu}{2}\left\|\boldsymbol{\varepsilon}(e_{\boldsymbol{u}}^i + e_{\boldsymbol{u}}^{i-1})\right\|^2 + \frac{\lambda}{4}\left\|\nabla\cdot(e_{\boldsymbol{u}}^i + e_{\boldsymbol{u}}^{i-1})\right\|^2 - \frac{\mu}{2}\left\|\boldsymbol{\varepsilon}(e_{\boldsymbol{u}}^i - e_{\boldsymbol{u}}^{i-1})\right\|^2 \\ - \frac{\lambda}{4}\left\|\nabla\cdot(e_{\boldsymbol{u}}^i - e_{\boldsymbol{u}}^{i-1})\right\|^2 + \frac{1}{M}\left\|e_{p_r}\right\|^2 \\ + \beta_{FS}(\left\|e_{p_r}^i\right\|^2 + \left\|e_{p_r}^i - e_{p_r}^{i-1}\right\|^2 - \left\|e_{p_r}^{i-1}\right\|^2) + \tau\langle \boldsymbol{K}^{-1} e_{\boldsymbol{w}_r}^i, e_{\boldsymbol{w}_r}^i\rangle = 0. \end{aligned} \tag{3.26}$$

Step 2: Mechanics
Now, we take the difference of iteration i and $i-1$ of (3.18e) and test with $\boldsymbol{v}_h = e_{\boldsymbol{u}}^i - e_{\boldsymbol{u}}^{i-1}$. Then

$$2\mu\left\|\boldsymbol{\varepsilon}(e_{\boldsymbol{u}}^i - e_{\boldsymbol{u}}^{i-1})\right\|^2 + \lambda\left\|\nabla\cdot(e_{\boldsymbol{u}}^i - e_{\boldsymbol{u}}^{i-1})\right\|^2 = \alpha\langle e_p^i - e_p^{i-1}, \nabla\cdot(e_{\boldsymbol{u}}^i - e_{\boldsymbol{u}}^{i-1})\rangle. \tag{3.27}$$

We add and subtract the terms on the right-hand side of (3.27) by $\gamma \in (0,1)$. This gives

$$\begin{aligned} 2\mu\left\|\boldsymbol{\varepsilon}(e_{\boldsymbol{u}}^i - e_{\boldsymbol{u}}^{i-1})\right\|^2 + \lambda\left\|\nabla\cdot(e_{\boldsymbol{u}}^i - e_{\boldsymbol{u}}^{i-1})\right\|^2 = \alpha\,\gamma\langle e_p^i - e_p^{i-1}, \nabla\cdot(e_{\boldsymbol{u}}^i - e_{\boldsymbol{u}}^{i-1})\rangle \\ + \alpha(1-\gamma)\langle e_p^i - e_p^{i-1}, \nabla\cdot(e_{\boldsymbol{u}}^i - e_{\boldsymbol{u}}^{i-1})\rangle. \end{aligned} \tag{3.28}$$

In the next few steps, we only look at the right-hand side of (3.28) to manipulate it as needed. Firstly, we apply Cauchy-Schwartz inequality (Lemma 3). Secondly, we apply the inequality (3.20). This yield

$$\begin{aligned}
&\alpha\,\gamma\langle e_p^i - e_p^{i-1}, \nabla\cdot(e_{\boldsymbol{u}}^i - e_{\boldsymbol{u}}^{i-1})\rangle + \alpha(1-\gamma)\langle e_p^i - e_p^{i-1}, \nabla\cdot(e_{\boldsymbol{u}}^i - e_{\boldsymbol{u}}^{i-1})\rangle \\
&\leq \alpha\,\gamma \left\|e_p^i - e_p^{i-1}\right\| \left\|\nabla\cdot(e_{\boldsymbol{u}}^i - e_{\boldsymbol{u}}^{i-1})\right\| + \alpha(1-\gamma)\left\|e_p^i - e_p^{i-1}\right\| \left\|\nabla\cdot(e_{\boldsymbol{u}}^i - e_{\boldsymbol{u}}^{i-1})\right\| \\
&\leq \sqrt{d}\;\alpha\,\gamma \left\|e_p^i - e_p^{i-1}\right\| \left\|\boldsymbol{\varepsilon}(e_{\boldsymbol{u}}^i - e_{\boldsymbol{u}}^{i-1})\right\| + \alpha(1-\gamma)\left\|e_p^i - e_p^{i-1}\right\| \left\|\nabla\cdot(e_{\boldsymbol{u}}^i - e_{\boldsymbol{u}}^{i-1})\right\|. \qquad (3.29)
\end{aligned}$$

We now combine (3.29) with (3.28):

$$\begin{aligned}
2\mu\left\|\boldsymbol{\varepsilon}(e_{\boldsymbol{u}}^i - e_{\boldsymbol{u}}^{i-1})\right\|^2 + \lambda\left\|\nabla\cdot(e_{\boldsymbol{u}}^i - e_{\boldsymbol{u}}^{i-1})\right\|^2 &\leq \sqrt{d}\;\alpha\,\gamma\left\|e_p^i - e_p^{i-1}\right\| \left\|\boldsymbol{\varepsilon}(e_{\boldsymbol{u}}^i - e_{\boldsymbol{u}}^{i-1})\right\| \\
&\quad + \alpha(1-\gamma)\left\|e_p^i - e_p^{i-1}\right\| \left\|\nabla\cdot(e_{\boldsymbol{u}}^i - e_{\boldsymbol{u}}^{i-1})\right\|.
\end{aligned}$$

Next, we apply Young's inequality (Lemma 4). Note that $\varepsilon_1' = 2\mu\varepsilon_1$ and $\varepsilon_2' = 2\lambda\varepsilon_2$ with $\varepsilon_1, \varepsilon_2, c > 0$. Also, we rearrange the terms and multiply both sides with a scaling constant c. Then

$$\begin{aligned}
c(2-\gamma\varepsilon_1)\mu\left\|\boldsymbol{\varepsilon}(e_{\boldsymbol{u}}^i - e_{\boldsymbol{u}}^{i-1})\right\|^2 + c(1-(1-\gamma)\varepsilon_2)\lambda\left\|\nabla\cdot(e_{\boldsymbol{u}}^i - e_{\boldsymbol{u}}^{i-1})\right\|^2 \\
\leq \frac{\alpha^2 c}{4}\left(\frac{d\gamma}{\mu\varepsilon_1} + \frac{1-\gamma}{\lambda\varepsilon_2}\right)\left\|e_p^i - e_p^{i-1}\right\|^2. \qquad (3.30)
\end{aligned}$$

We choose the parameters optimal by minimizing

$$\min_{\gamma, c, \varepsilon_1, \varepsilon_2} \frac{\alpha^2 c}{4}\left(\frac{\gamma d}{\mu\varepsilon_1} + \frac{1-\gamma}{\lambda\varepsilon_2}\right), \qquad (3.31)$$

such that

$$\begin{aligned}
c, \varepsilon_1, \varepsilon_2 &> 0, \\
\gamma &\in (0,1), \\
c(2-\gamma\varepsilon_1) &= \frac{1}{2}, \qquad (3.32) \\
c(1-(1-\gamma)\varepsilon_2) &= \frac{1}{4}. \qquad (3.33)
\end{aligned}$$

Here, (3.32)-(3.33) are limited by (3.26). In other words, we want $\frac{\mu}{2}$ in front of $\left\|\boldsymbol{\varepsilon}(e_{\boldsymbol{u}}^i - e_{\boldsymbol{u}}^{i-1})\right\|^2$ and $\frac{\lambda}{4}$ in front of $\left\|\nabla\cdot(e_{\boldsymbol{u}}^i - e_{\boldsymbol{u}}^{i-1})\right\|^2$ as in (3.26). We rearrange (3.32) and (3.33) such that we

achieve expressions for $1/\varepsilon_1$ and $1/\varepsilon_2$:

$$\frac{1}{\varepsilon_1} = \frac{\gamma}{2(1-\frac{1}{c})}, \tag{3.34}$$

$$\frac{1}{\varepsilon_2} = \frac{1-\gamma}{2(1-\frac{1}{2c})}. \tag{3.35}$$

After inserting (3.34)-(3.35) in (3.31), the minimization problem only depends on γ and c. It now reads

$$\min_{\gamma,c} \frac{\alpha^2 c}{4(1-\frac{1}{4c})}\left(\frac{d\gamma^2}{2\mu} + \frac{(1-\gamma)^2}{\lambda}\right), \tag{3.36}$$

such that $c > \frac{1}{4}$ and $\gamma \in (0,1)$. We obtain expression for γ and c from (3.36). These expression are inserted in (3.34)-(3.35) to obtain optimal values for ε_1 and ε_2. All the optimal values read

$$c^* = \frac{1}{2},$$

$$\gamma^* = \frac{2\mu}{2\mu + d\lambda},$$

$$\varepsilon_1^* = \frac{2\mu + d\lambda}{2\mu},$$

$$\varepsilon_2^* = \frac{2\mu + d\lambda}{2d\lambda}.$$

We insert the optimal values in (3.30). Then

$$\frac{\mu}{2}\left\|\boldsymbol{\varepsilon}(e_{\boldsymbol{u}}^i - e_{\boldsymbol{u}}^{i-1})\right\|^2 + \frac{\lambda}{4}\left\|\nabla\cdot(e_{\boldsymbol{u}}^i - e_{\boldsymbol{u}}^{i-1})\right\|^2 \leq \frac{\alpha^2}{4(\frac{2}{d}\mu+\lambda)}\left\|e_p^i - e_p^{i-1}\right\|^2. \tag{3.38}$$

Step 3: Darcy with singularity removal

Here, we start by taking the difference between (3.18b) and (3.17c). This yields

$$\langle \boldsymbol{K}^{-1} e_{\boldsymbol{w}_r}^i, \boldsymbol{z}_h\rangle - \langle e_{p_r}^i, \nabla\cdot\boldsymbol{z}_h\rangle = 0.$$

Next, we use $\nabla\cdot\tilde{\boldsymbol{z}}_h = q_h$ from Thomas' Lemma (Lemma 6):

$$\langle \boldsymbol{K}^{-1} e_{\boldsymbol{w}_r}^i, \tilde{\boldsymbol{z}}_h\rangle - \left\|e_{p_r}^i\right\|^2 = 0.$$

We now apply Cauchy-Schwartz inequality and rearrange:

$$\left\|e_{p_r}^i\right\|^2 \leq \langle \boldsymbol{K}^{-1} e_{\boldsymbol{w}_r}^i, e_{\boldsymbol{w}_r}^i\rangle^{1/2} \langle \boldsymbol{K}^{-1}\tilde{\boldsymbol{z}}_h, \tilde{\boldsymbol{z}}_h\rangle^{1/2}.$$

First, we apply (A7). Second, we use $\|\boldsymbol{z}_h\| \leq C_{\Omega,d} \|q_h\|$ from Thomas' Lemma. Third, we square both sides and rearrange. This reads

$$\begin{aligned}\left\|e^i_{p_r}\right\|^2 &\leq \frac{1}{\sqrt{k_m}} \langle \boldsymbol{K}^{-1} e^i_{\boldsymbol{w}_r}, e^i_{\boldsymbol{w}_r} \rangle^{1/2} \|\tilde{\boldsymbol{z}}_h\| \\ &\leq \frac{C_{\Omega,d}}{\sqrt{k_m}} \langle \boldsymbol{K}^{-1} e^i_{\boldsymbol{w}_r}, e^i_{\boldsymbol{w}_r} \rangle^{1/2} \left\|e^i_{p_{r,h}}\right\|,\end{aligned}$$

$$\frac{k_m}{C^2_{\Omega,d}} \left\|e^i_{p_r}\right\|^2 \leq \langle \boldsymbol{K}^{-1} e^i_{\boldsymbol{w}_r}, e^i_{\boldsymbol{w}_r} \rangle. \tag{3.39}$$

Step 4: Combining Step 1-3

Substituting (3.38) and (3.39) into (3.26), and then rearrange:

$$\begin{aligned}\frac{\mu}{2} \left\|\boldsymbol{\varepsilon}(e^i_{\boldsymbol{u}} + e^{i-1}_{\boldsymbol{u}})\right\|^2 + \frac{\lambda}{4} \left\|\nabla \cdot (e^i_{\boldsymbol{u}} + e^{i-1}_{\boldsymbol{u}})\right\|^2 + \left(\frac{1}{M} + \frac{\beta_{FS}}{2} + \frac{k_m \tau}{C^2_{\Omega,d}}\right) \left\|e^i_{p_r}\right\|^2 \\ + \frac{\beta_{FS}}{2} \left\|e^i_{p_r} - e^{i-1}_{p_r}\right\|^2 \leq \frac{\beta_{FS}}{2} \left\|e^{i-1}_{p_r}\right\|^2 + \frac{\alpha^2}{4(\frac{2}{d}\mu + \lambda)} \left\|e^i_{p_r} - e^{i-1}_{p_r}\right\|^2.\end{aligned} \tag{3.40}$$

We can discard the two first positive terms in (3.40) since the inequality in (3.40) still holds without them. This leaves

$$\left(\frac{1}{M} + \frac{\beta_{FS}}{2} + \frac{k_m \tau}{C^2_{\Omega,d}}\right) \left\|e^i_{p_r}\right\|^2 + \frac{\beta_{FS}}{2} \left\|e^i_{p_r} - e^{i-1}_{p_r}\right\|^2 \leq \frac{\beta_{FS}}{2} \left\|e^{i-1}_{p_r}\right\|^2 + \frac{\alpha^2}{4(\frac{2}{d}\mu + \lambda)} \left\|e^i_{p_r} - e^{i-1}_{p_r}\right\|^2.$$

Providing that $\beta_{FS} \leq \frac{\alpha^2}{2(\frac{2}{d}\mu + \lambda)}$ holds, i.e. (3.21), we have:

$$\left(\frac{1}{M} + \frac{\beta_{FS}}{2} + \frac{k_m \tau}{C^2_{\Omega,d}}\right) \left\|e^i_{p_r}\right\|^2 \leq \frac{\beta_{FS}}{2} \left\|e^{i-1}_{p_r}\right\|^2,$$

which proves (3.22).

Step 5: Mechanics revisited

We return to the mechanics equation one last time. We subtract (3.18e) from (3.17a) and test

with $\boldsymbol{v}_h = e^i_{\boldsymbol{u}}$. This yields

$$2\mu \left\|\boldsymbol{\varepsilon}(e^i_{\boldsymbol{u}})\right\|^2 + \lambda \left\|\nabla \cdot e^i_{\boldsymbol{u}}\right\|^2 = \alpha \langle e^i_p, \nabla \cdot e^i_{\boldsymbol{u}} \rangle.$$

Here, we repeat all steps in Step 2, but due to linearity we analogously obtain

$$\frac{\mu}{2} \left\|\boldsymbol{\varepsilon}(e^i_{\boldsymbol{u}})\right\|^2 + \frac{\lambda}{4} \left\|\nabla \cdot e^i_{\boldsymbol{u}}\right\|^2 \leq \frac{\alpha^2}{4(\frac{2}{d}\mu + \lambda)} \left\|e^i_p\right\|^2.$$

This proves (3.23).

Step 6: Spitting of pressure and flux
We subtract (3.17d) from (3.18c) This yields

$$e_p = e_{p_r},$$

which is (3.24). Next, we subtract (3.17e) from (3.18d). Then

$$e_{\boldsymbol{w}} = e_{\boldsymbol{w}_r},$$

which is the same as (3.25).

We finish up the proof by using the Banach contraction argument to prove that the method is a contradiction. By Banach fixed-point theorem, the method converges if

$$\beta_{FS} = \frac{\alpha^2}{2(\frac{2}{d}\mu + \lambda)} < 1,$$

and is a contraction since

$$\beta_{FS} < 1.$$

Hence, the method also has a unique fixed point. □

Chapter 4

Numerical simulations

The aim of this thesis has been to develop a mathematical model to obtain optimal convergence for solving coupled flow and mechanics equations at the level of microcirculation. We will in this chapter numerically verify the theoretically results from Theorem 7. We recall our system of equations:

$$-\nabla\cdot[2\mu\boldsymbol{\varepsilon}(\boldsymbol{u})+\lambda(\nabla\cdot\boldsymbol{u})\boldsymbol{I}]+\alpha\nabla p=\boldsymbol{f}, \tag{4.1a}$$

$$\partial_t\left(\frac{p}{M}+\alpha\,\nabla\cdot\boldsymbol{u}\right)+\nabla\cdot\boldsymbol{w}=\psi+f\delta_\Gamma, \tag{4.1b}$$

$$\frac{\boldsymbol{w}}{K}+\nabla p=0. \tag{4.1c}$$

We assume (A1)-(A4), and consequently K is a positive scalar quantity and $\boldsymbol{g}$ is neglected. To obtain optimal convergence for solving (4.1a)-(4.1c), we introduced a singularity removal-based scheme in Section 3.2.3. It combines two techniques: one splitting technique [Gjerde et al., 2019, 2018] and second the fixed-stress splitting scheme. We recall that the solutions of p and $\boldsymbol{w}$ can be split into one low and one high regularity term denoted by the subscript s and r, i.e.

$$p=p_s+p_r, \tag{4.2a}$$

$$\boldsymbol{w}=\boldsymbol{w}_s+\boldsymbol{w}_r, \tag{4.2b}$$

respectively. We first reformulate (4.1b)-(4.1c) to solve for p_r and $\boldsymbol{w}_r$. Then the fixed-stress splitting scheme is applied in order to solve the system of equations in three step. First, solving (4.1b)-(4.1c) to get p_r and $\boldsymbol{w}_r$. Secondly, interpolating p_s onto the discrete space of the pressure to obtain the actual pressure. Lastly, (4.1a) is solved with the reconstructed pressure to get $\boldsymbol{u}$.

Finally, we simulate flow and mechanics with a data set describing a vascular system of a human brain. The data set consists of arteries and veins represented by line segments. Moreover, the code is implemented with FEniCS [Alnæs et al., 2015] and all plots are obtained with ParaView [Ahrens et al., 2005].

4.1 Numerical examples in 2D

In this section, we set the parameters for the problem such that the solutions are independent of the z-axis. We also let $f \in H^2(\Omega)$. Then we can reduce our problem to two dimensions. Note that we assume (A1)-(A4). Furthermore, we perform convergence tests on the following test problems:

Test cases in 2D:
4.1.1: Test case with smooth right-hand sides.
4.1.2: Test case with a point source.
4.1.3: Test case with a point source solved by the fixed-stress splitting scheme with singularity removal.

In all applications in 2D, we consider the unit square mesh:

$$\Omega = \{(0,1) \times (0,1) \subset \mathbb{R}^2\}.$$

For the choice of f, we have in mind that the flow of blood from the heart has a pulsative nature. Therefore, we want to test the convergence of the method with $f(t)$ as a pulsating function. We set

$$f(t) = \sin(t). \tag{4.3}$$

μ and λ are respectively given by functions of the bulk modulus E and Poisson's ratio ν:

$$\mu = \frac{E}{2(1+\nu)}, \tag{4.4}$$

$$\lambda = \frac{E\nu}{(1+\nu)(1-2\nu)}. \tag{4.5}$$

The Poisson's ratio ν is very close to $1/2$ for nearly incompressible material [Ern and Guermond, 1992], where we set $\nu = 0.4999$ for all cases. Furthermore, the tuning parameter, which theoretically gives optimal convergence rates, was found by the proof of convergence

in Section 3.3, i.e.

$$\beta_{FS} = \frac{\alpha^2}{2(\frac{2\mu}{d} + \lambda)}. \tag{4.6}$$

Before turning to our numerical examples, we recall the short-hand notation for the induced norm:

$$\|u\|_{L^2(\Omega)} = \|u\|_{L^2}.$$

Table 4.1 Parameters for numerical examples in two dimensions.

Symbol:	Quantity:	Value:
K	Permeability scalar divided by ν_f	1.0 D/P
E	Bulk modulus	1.0 Pa
M	Biot modulus	1.0 Pa
α	Biot-Willis coefficient	1.0
ν	Poisson's ratio	0.4999
$\boldsymbol{g}$	Gravitational vector	$\mathbf{0}$ m/s^2
T	Final time	1.0 s
τ	Time step	0.1 s
h	Mesh size	$1/8,\ 1/16,\ 1/32,\ 1/64$
ε_a	Absolute error tolerance	$1e-6$
ε_r	Relative error tolerance	$1e-6$

4.1.1 Test case with smooth right-hand sides

The analytic solutions in the first test case were taken as in [Both et al., 2017] and is commonly used as a test case in literature. We let $f = 0$, which yields smooth right-hand sides. Furthermore, (4.1a)-(4.1c) are solved by the fixed-stress splitting scheme, i.e. (3.12a)-(3.12c). This test case was included as a reference case. The parameters considered are summarized in Table 4.1. Moreover, the analytic solutions read

$$p = tx(1-x)y(1-y), \qquad \boldsymbol{w} = -K\,\nabla p, \qquad \boldsymbol{u} = tx(1-x)y(1-y)\,[1,1]^T.$$

Table 4.2 shows the errors and the convergence rates for this test problem. It can be observed that all solutions obtained optimal convergence rates. For simplicity, let the subscript a denote the analytic solutions and the subscript h denote the numerical solutions. Moreover, all plots of the solutions from this case are shown in Figure 4.1, where the plots of $\boldsymbol{w}_h$ and $\boldsymbol{u}_h$

are of the magnitude.

Table 4.2 Errors and convergence rates obtained when applying the fixed-stress splitting scheme to a test problem with all smooth variables. For reference, optimal convergence rates are listed in the bottom row.

h	$\|\boldsymbol{p}_a - \boldsymbol{p}_h\|_{L^2}$	$\|\boldsymbol{w}_a - \boldsymbol{w}_h\|_{L^2}$	$\|\boldsymbol{u}_a - \boldsymbol{u}_h\|_{L^2}$
$1/8$	$4.4e-03$	$1.8e-02$	$2.1e-03$
$1/16$	$2.2e-03$	$9.3e-03$	$5.4e-04$
$1/32$	$1.1e-03$	$4.7e-03$	$1.4e-04$
$1/64$	$5.5e-04$	$2.3e-03$	$3.4e-05$
Rate	1.0	1.0	2.0
Optimal	1.0	1.0	2.0

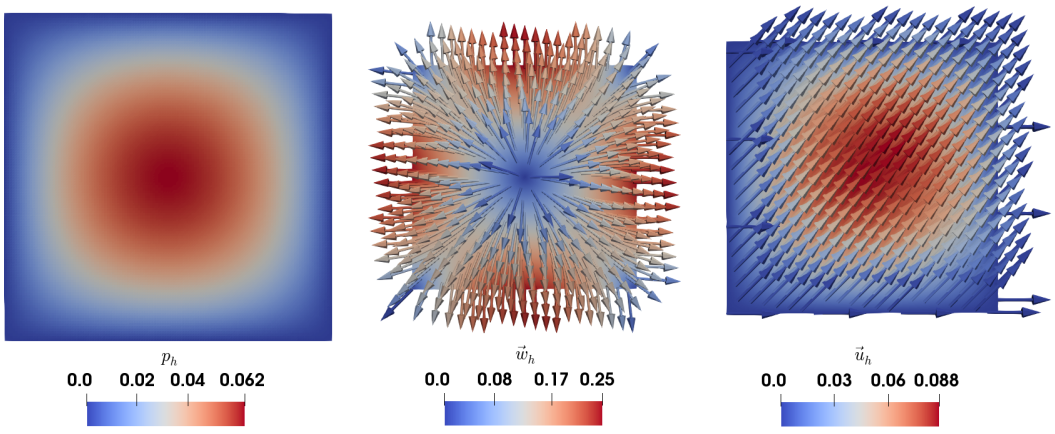

(a) (b) (c)

Fig. 4.1 Numerical solutions obtained when applying the fixed-stress splitting scheme to a test problem with smooth right-hand sides: Pressure (a), magnitude of the flux (b), and magnitude of the displacement (c).

4.1.2 Test case with a point source

We let $f(t)$ be given by (4.3) and δ_Γ be a point source. Then we solve (4.1a)-(4.1c) with the standard fixed-stress splitting scheme, i.e. (3.12a)-(3.12c). We recall that suboptimal convergence rates were found to be local to Γ for a 3D problem with 1D line sources [Gjerde et al., 2018; Köppl et al., 2016]. Optimal convergence was retrieved when removing a small region surrounding the neighborhood of Γ. We test this for the Biot model. In other words, we will solve (4.1a)-(4.1c) with the fixed-stress splitting scheme and ignore a small region R when calculating the errors of $\boldsymbol{w}$ and $\boldsymbol{u}$. R is given by (2.12) and illustrated in Figure 2.1.

We kept the displacement from the previous test case. The parameters are summarized in Table 4.1. We also recall that $p_s = \frac{fG}{K}$, where G given by (1.15). We set $p_r = 0$. Then the analytic solutions read

$$p = -\frac{1}{2\pi K}\left(\sin(t)\ln(r)\right) \qquad \boldsymbol{w} = -K\,\nabla p \qquad \boldsymbol{u} = tx(1-x)y(1-y)\,[1,1]^T.$$

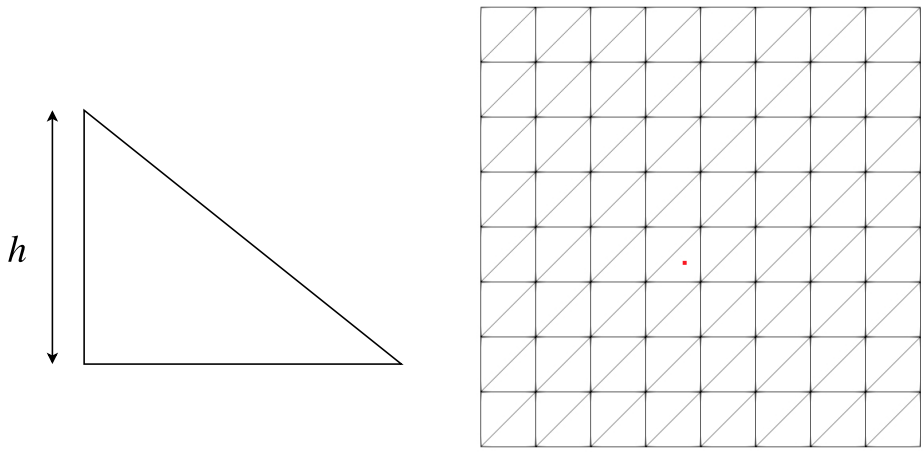

(a) (b)

Fig. 4.2 Illustration of the mesh size h of a triangle element (a), and the position of the point source with respect to the mesh (b). The uniform mesh is constructed by dividing the unit square into $1/h \times 1/h$ squares and dividing each square by the diagonal. The mesh size of the unit square mesh is the length of the shortest side of the triangle.

The mesh size of a triangle element is illustrated in Figure 4.2(a). We set the point source in the origin of the mesh, but as illustrated in Figure 4.2(b), the point source moved to the

center of one of the surrounding elements.

The errors and the convergence rates obtained for this test case are shown in Table 4.3. For simplicity, we let the subscript a indicates the analytical solutions and the subscript h the numerical solutions. We can observe in Table 4.3 that the convergence rates for $\boldsymbol{w}$ increased when ignoring the small region before calculating the errors and became close to optimal. The convergence rates of p was decreasing with the mesh size.

Table 4.3 Errors and convergence rates obtained with the fixed-stress splitting scheme to a test problem with a point source. Optimal convergence rates are listed in the bottom row.

h	$\|\boldsymbol{p}_a - \boldsymbol{p}_h\|_{L^2}$	$\|\boldsymbol{w}_a - \boldsymbol{w}_h\|_{L^2}$	$\left\|\boldsymbol{w}_{R,a} - \boldsymbol{w}_{R,h}\right\|_{L^2}$	$\|\boldsymbol{u}_a - \boldsymbol{u}_h\|_{L^2}$	$\left\|\boldsymbol{u}_{R,a} - \boldsymbol{u}_{R,h}\right\|_{L^2}$
$1/16$	$1.1e-01$	$5.2e-01$	$4.2e-01$	$2.5e-04$	$2.9e-04$
$1/32$	$5.6e-02$	$5.2e-01$	$2.3e-01$	$6.1e-05$	$7.3e-05$
$1/64$	$3.2e-02$	$5.2e-01$	$1.2e-01$	$1.5e-05$	$1.8e-05$
Rate	0.9	0.0	0.9	2.0	2.0
Optimal	1.0	1.0	1.0	2.0	2.0

Plots of the numerical and analytic solutions are shown in Figure 4.3-4.4. The plots of the pressure and the flux have qualitative differences. We cropped these plots to provide a closeup look at this region. As stated earlier, there are difficulties in numerically resolving the solutions in the neighborhood of Γ. This is illustrated in the plots in Figure 4.3.

Figure 4.3(a)-(b) show plots of p_a and p_h, respectively. Even though the pressure obtained optimal convergence, the plots of p_a and p_h have qualitative differences. The differences in these figures are the intensity and the size in the region surrounding Γ, where p_a has both a larger distributed region and intensity. The reason for these differences can be difficulties resolving the singularity when interpolating the numerical solution of the pressure. Furthermore, Figure 4.3(c)-(d) show the plots of the magnitude of $\boldsymbol{w}_a$ and $\boldsymbol{w}_h$, respectively. The shape of the flux in Figure 4.3(c) is expected to look similar the function $1/r$, but before plotting, the variable is interpolated onto elements in $\mathbb{RT}_0$. These elements are defined for functions in $H(div;\Omega)$. Though, the flux itself does not even belong to $L^2(\Omega)$. Recall that the functions in $H(div;\Omega)$ should themselves be in $L^2(\Omega)$ and their divergence should also be in $L^2(\Omega)$. Thus, the singularity makes it difficult to interpolate the flux. This can be illustrated in the plots of the analytic and numerical solutions of the flux in Figure 4.3(c)-(d),

respectively.

Lastly, Figure 4.4 shows uncropped plots of both the analytical and the numerical solutions, respectively. Figure 4.4(a)-(b) shows the plots of the pressure. Accordingly, Figure 4.4(c)-(e) shows plots of the magnitude of $\boldsymbol{w}_a$, $\boldsymbol{w}_h$ and $\boldsymbol{u}_h$ including vector fields.

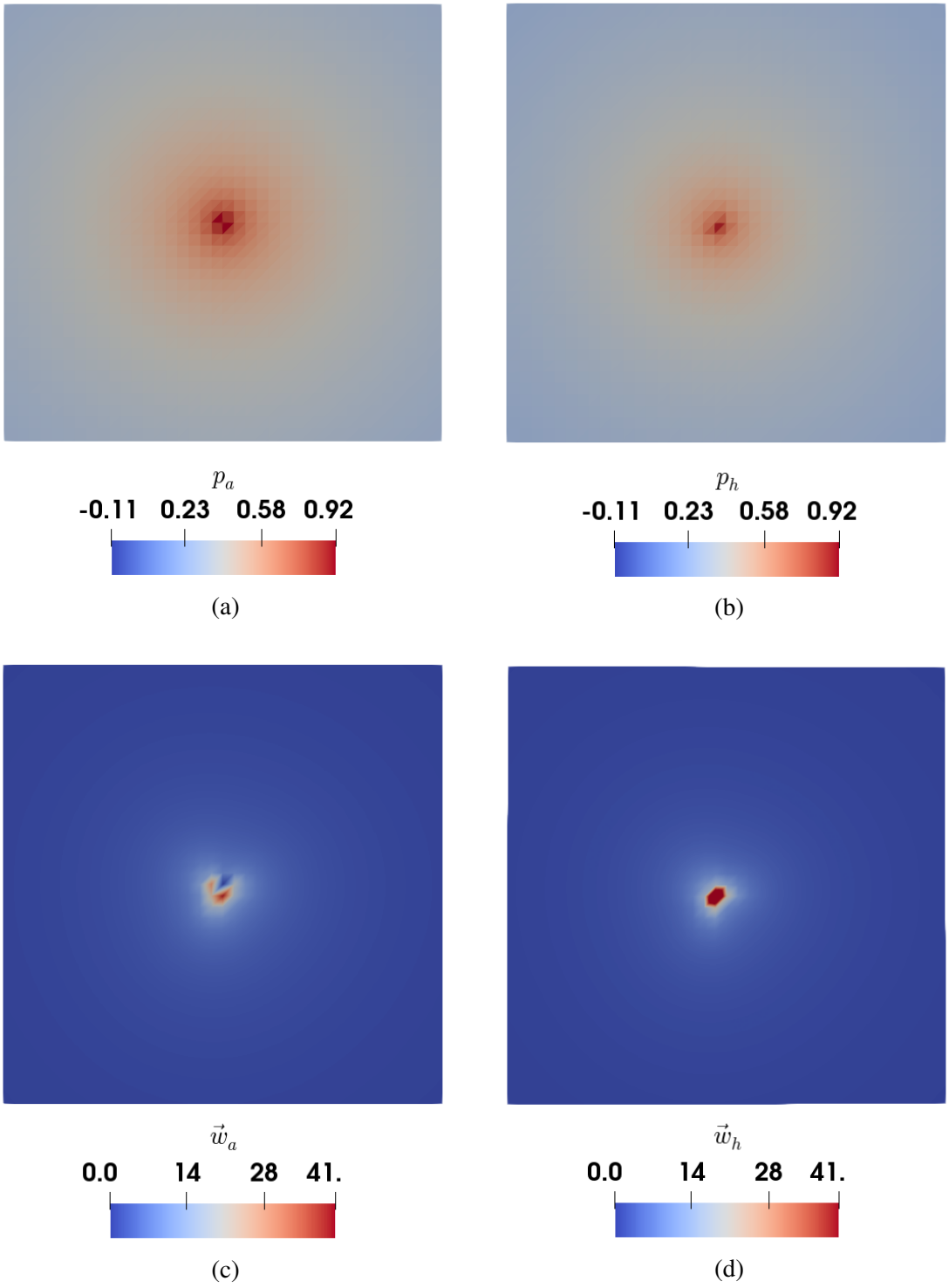

Fig. 4.3 Upper line: Cropped plots of the pressure; analytic (a) and numerical (b). Lower line: Cropped plots of the magnitude of the flux; analytic (c) and numerical (d). These plots were obtained for a test problem solved by the fixed-stress splitting scheme with a point source.

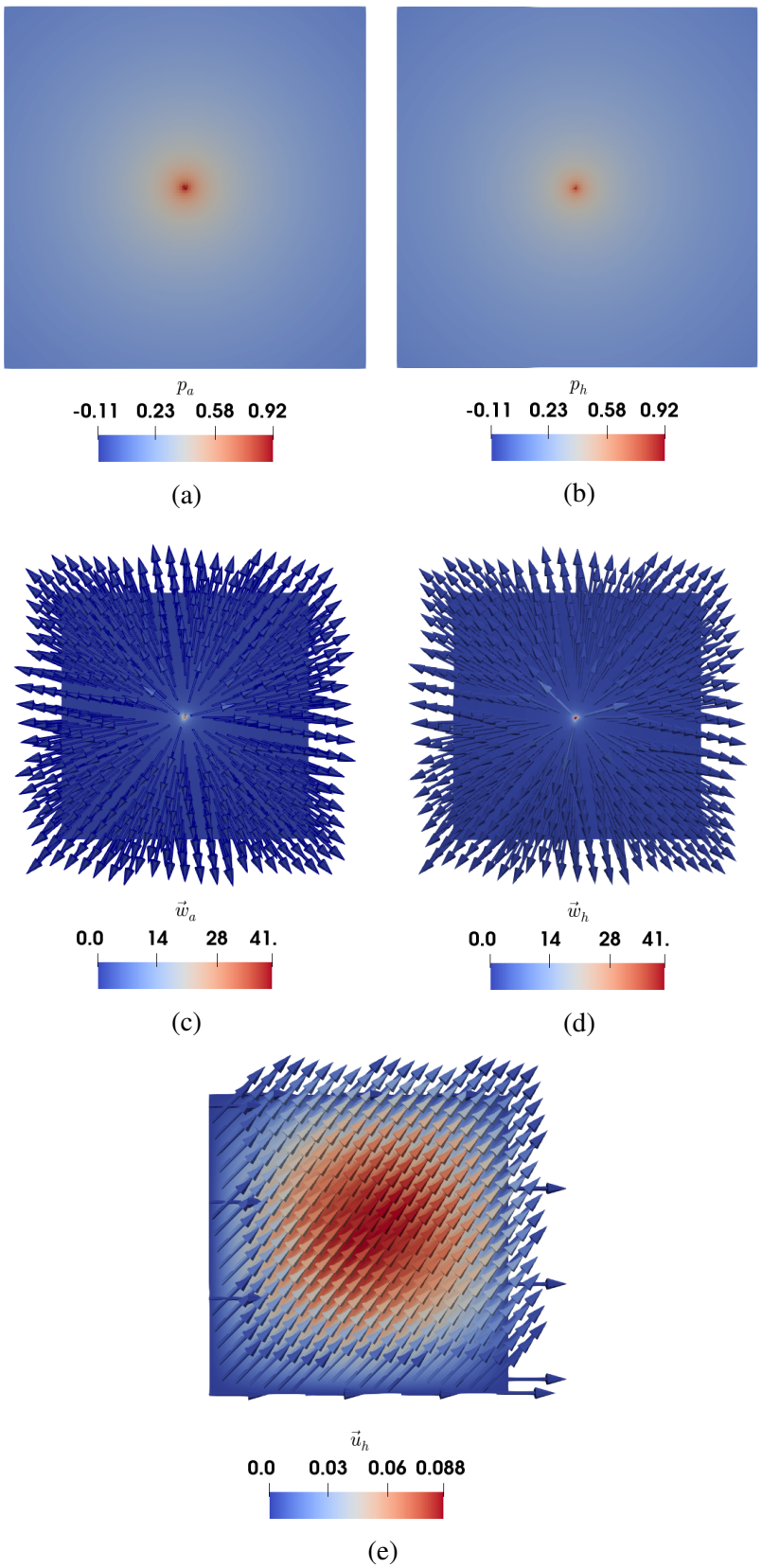

Fig. 4.4 Upper line: Plots of the pressure; analytic (a) and numerical (b). Middle line: Plots of the magnitude of the flux; analytic (c) and numerical (d). Lower line: Plot of the magnitude of the displacement; numerical (e). All plots are numerical solutions obtained by fixed-stress splitting scheme with a point source.

4.1.3 Test case with a point source solved by the fixed-stress splitting scheme with singularity removal

In last test case in 2D, we numerically verify the theoretically results from Theorem 7 for $d = 2$. As in the test case in Section 4.1.2, we let δ_Γ be a point source. Then we solve (4.1a)-(4.1c) by the fixed-stress splitting scheme with singularity removal. This scheme was introduced in Section 3.2.3 and is given by (3.18a)-(3.18e). The motivation to use this method is that the Dirac source term causes the solutions of p and $\boldsymbol{w}$ to be singular. This leads to difficulties in resolving the solutions numerically. The previous test case illustrates the lack of convergence in the $L^2(\Omega)$-norm of the flux. This is illustrated in Table 4.3. We also observed that the lack of convergence was highly related to the neighborhood of the point source. Therefore, there is an interest in a singularity removal-based scheme.

The fixed-stress splitting scheme with singularity removal can be explained in a few sentences. The scheme is based on splitting the solutions of the pressure and the flux into one explicit, low regularity term, which captures the singularity, and one implicit, higher regularity term. The unknown is the high regularity term, and the low regularity term is given. The actual pressure and flux are obtained by (4.2a)-(4.2b), respectively. The flow equations are reformulated in order to solve for the high regularity terms. The developed scheme consists of three steps. First, it solves (4.1b)-(4.1c) to get p_r and $\boldsymbol{w}_r$. Second, p_s and $\boldsymbol{w}_s$ are interpolated onto the discrete space of the pressure and the flux to reconstruct the actual pressure and flux. Third, solving (4.1a) with the reconstructed p to obtain $\boldsymbol{u}$.

We recall from Section 2.2.1 that $p_s = \frac{fG}{K}$. Then we have $p_s = \frac{\sin(t)G}{K}$, where G is given by (1.15). The parameters used are summarized in Table 4.1. The analytic solutions then read:

$$p_r = -\frac{x\,y\,t}{2\pi K} \qquad \boldsymbol{w}_r = -K\,\nabla p_r \qquad \boldsymbol{u} = \frac{t}{2\pi}[\cos(x),\ \sin(y)]^T.$$

Table 4.4 Errors and convergence rates obtained with a point source. The results are obtained by solving the system of equations by the fixed-stress splitting scheme with singularity removal. Optimal convergence rates are listed in the bottom row.

h	$\left\|\boldsymbol{p}_{r,a}-\boldsymbol{p}_{r,h}\right\|_{L^2}$	$\left\|\boldsymbol{w}_{r,a}-\boldsymbol{w}_{r,h}\right\|_{L^2}$	$\left\|\boldsymbol{u}_a-\boldsymbol{u}_h\right\|_{L^2}$
$1/8$	$4.3e-03$	$8.1e-03$	$2.3e-04$
$1/16$	$2.1e-03$	$4.1e-03$	$5.7e-05$
$1/32$	$1.1e-03$	$2.0e-03$	$1.4e-05$
$1/64$	$5.4e-04$	$1.0e-03$	$3.5e-06$
Rate	1.0	1.0	2.0
Optimal	1.0	1.0	2.0

The error estimates and the convergence rates are shown in Table 4.4. We obtained optimal convergence rates for all variables solved with this scheme. Furthermore, in Figure 4.5, we can observe different impacts from the low and high regularity terms in the total solutions of the pressure and flux. We only included the numerical solutions since the analytic and numerical results were close to identical. Figure 4.5(a)-(c) shows the plots of $p_{r,h}$, $p_{s,h}$ and p_h, respectively. In addition, Figure 4.5(d)-(f) shows the plots of the magnitude of $\boldsymbol{w}_{r,h}$, $\boldsymbol{w}_{s,h}$ and $\boldsymbol{w}_h$, accordingly. Lastly, Figure 4.5(g) shows the plot of the magnitude of u_h.

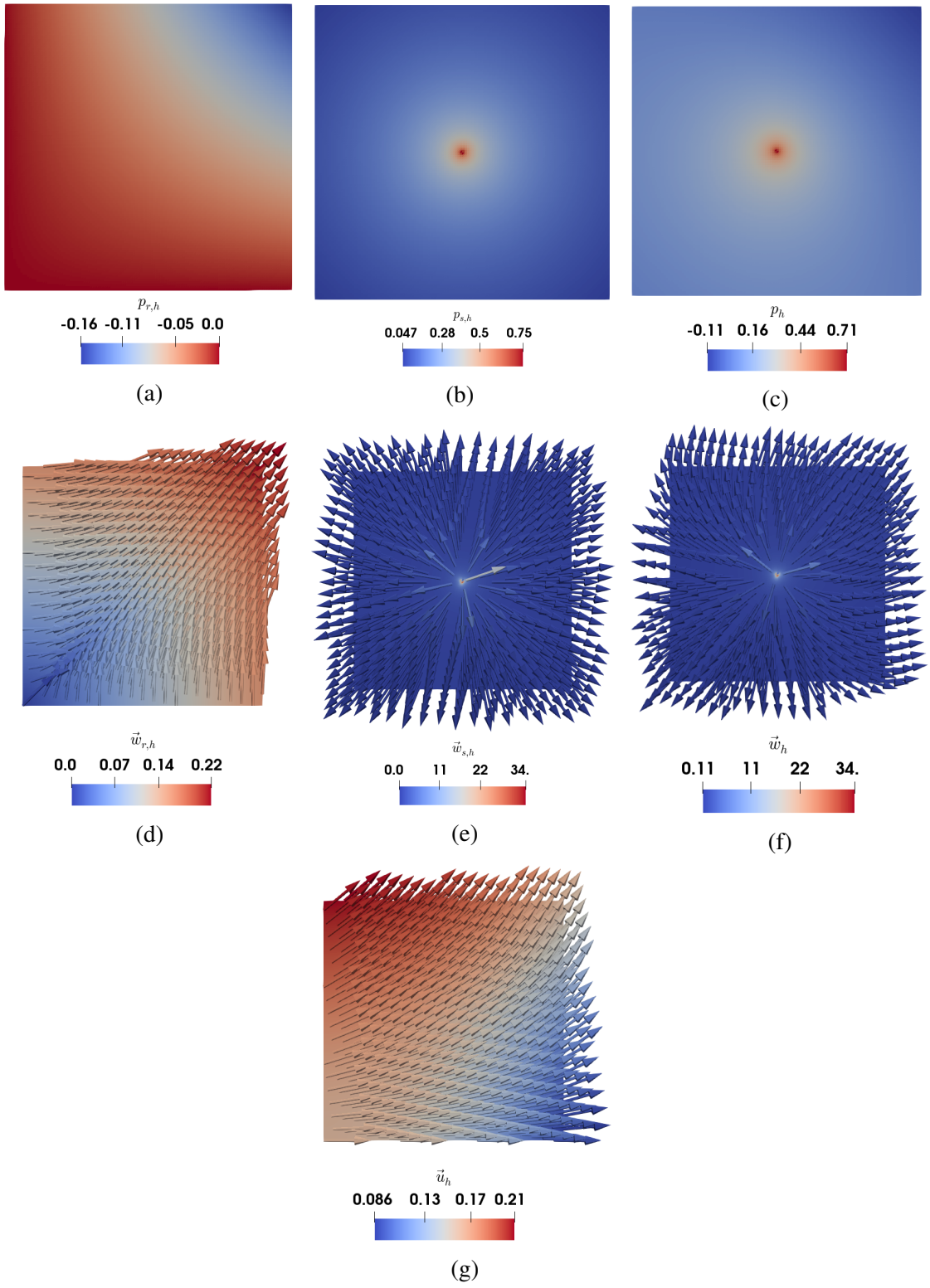

Fig. 4.5 Upper line: Plots of the pressure; the low regularity term (a), the high regularity term (b) and the reconstructed pressure (c). Middle line: Plots of the magnitude of the flux; the low regularity term (d), the high regularity term (e) and the reconstructed flux (f). Lower line: Plot of the magnitude of the displacement; the displacement (g). All plots are numerical solutions obtained by fixed-stress splitting scheme with singularity removal with a point source.

4.2 Numerical simulations in 3D

This chapter concludes with numerical simulations in 3D. We will first numerically verify the theoretical results from Theorem 7 for $d = 3$. We recall that Section 4.1.2 showed optimal convergence rates for $d = 2$. Finally, we perform simulations of flow and mechanics for a data set describing a vascular system of a human brain. That is, numerical simulation on a data set with complex geometry. We solve (4.1a)-(4.1c) with the fixed-stress splitting scheme with singularity removal, i.e. (3.18a)-(3.18e). Furthermore, we consider the unit cube mesh for all applications in this section:

$$\Omega = \{(0,1) \times (0,1) \times (0,1) \subset \mathbb{R}^3\}.$$

We let μ, λ and β_{FS} be given by (4.4)-(4.6), respectively. Note that we assume (A1)-(A4). To summarize, we consider the following simulations in 3D:

Simulations in 3D:
4.2.1: Test case with a line source.
4.2.2: Simulation of flow and mechanics in a non-trivial data set.

Table 4.5 Parameters for simulations in three dimensions.

Symbol:	Quantity:	Value:
K	Permeability scalar divided by ν_f	0.5 D/P
E	Tuning parameter	1.0 Pa
M	Biot modulus	1.0 Pa
α	Biot coefficient	1.0
ν	Poisson's ratio	0.4899, 0.4999
$\boldsymbol{g}$	Gravitational vector	$\mathbf{0}$ m/s^2
T	Final time	1.0 s
τ	Time step	0.1 s
h	Mesh size	$1/2$, $1/4$, $1/8$, $1/16$
ε_a	Absolute error tolerance	$1e-6$
ε_r	Relative error tolerance	$1e-6$

4.2.1 Test case with a line source

In this section, we numerically verify the theoretically results from Theorem 7 for $d = 3$. We let δ_Γ be a line source. Then we solve (4.1a)-(4.1c) by the fixed-stress splitting scheme with singularity removal. We let $f(s_j,t) \in H^2(\Gamma_j)$, where s_j is the arc-length of the line segment j and t the time. With the same intention as in Section 4.1, i.e. (4.3), we set f to be a pulsative function:

$$f(s_j,t) = \sin(t)(1+s_j). \tag{4.7}$$

The analytic solutions of this test problem was set to:

$$p_r = \frac{1}{4\pi K}\mathrm{d}_s f(s,t)(r_a - r_b) \qquad \boldsymbol{w}_r = -K\nabla p_r \qquad \boldsymbol{u} = tx(1-x)y(1-y)z(1-z)[1,1,1]^T.$$

We recall that $r_a = \|\boldsymbol{x}-\boldsymbol{a}\|$ and $r_b = \|\boldsymbol{x}-\boldsymbol{b}\|$, where $\boldsymbol{a}$ and $\boldsymbol{b}$ are the points between the line segment. This is also illustrated in Figure 2.1. Furthermore, Figure 4.6 illustrates a tetrahedron element, its mesh size and the position of the line source with respect to the element. The position of the line source with respect to the mesh is same as for the point source in Section 4.1. This is illustrated in Figure 4.2(b). The parameters for this test problem are summarized in Table 4.5. We also recall the short-hand notation for the induced norm

$$\|u\|_{L^2(\Omega)} = \|u\|_{L^2}.$$

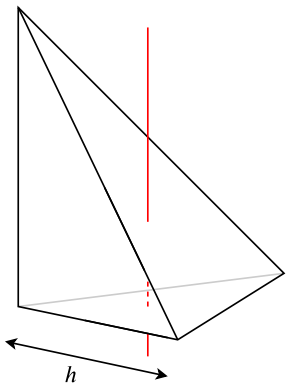

Fig. 4.6 Illustration of a tetrahedron element. The uniform cube is constructed by dividing the unit cube into $1/h \times 1/h \times 1/h$ cubes and dividing each cube by the diagonal. The mesh size for the unit cube mesh are the length of the shortest side of the tetrahedron. The red line illustrates a line source going through the center of the tetrahedron.

Table 4.6 Errors and convergence rates obtained with the fixed-stress splitting scheme with singularity removal to a test problem with a line source. The results are obtained with $\nu = 0.4999$, and $\mathbb{CG}_1$ elements for the displacements. Optimal convergence rates are demonstrated in the bottom row.

h	$\left\|\boldsymbol{p}_{r,a} - \boldsymbol{p}_{r,h}\right\|_{L^2}$	$\left\|\boldsymbol{w}_{r,a} - \boldsymbol{w}_{r,h}\right\|_{L^2}$	$\|\boldsymbol{u}_a - \boldsymbol{u}_h\|_{L^2}$	Rates for $\boldsymbol{u}$
$1/2$	$1.5e-02$	$2.8e-02$	$5.3e-03$	
$1/4$	$8.0e-03$	$1.3e-02$	$1.5e-03$	1.9
$1/8$	$4.0e-03$	$7.2e-03$	$4.1e-04$	1.8
$1/16$	$2.0e-03$	$3.5e-03$	$2.3e-04$	0.8
Rate	1.0	1.0	1.2	
Optimal	1.0	1.0	2.0	

For simplicity, let the subscript h indicate the numerical solution and the subscript a indicate analytical solution. We observe in Table 4.6 that $\boldsymbol{u}$ does not converge of order h^2. Hence, we tested with $\nu = 0.4899$ since further testing revealed that this parameter had a significant impact of the errors of $\boldsymbol{u}$. The errors of p and $\boldsymbol{w}$ were excluded due to obtaining the same results for both variables. The reason for the lack of optimal convergence of $\boldsymbol{u}$ may be that the singularity from p is hard to resolve when solving the mechanics equation in 3D.

Table 4.7 Errors and the convergence rates obtained with the fixed-stress splitting scheme with singularity removal to a test problem with a line source. Results obtained with $\mathbb{CG}_1$ elements and for $\nu = 0.4899$ [Zakerzadeh and Zunino, 2015]. The optimal convergence rate is demonstrated in the bottom row.

h	$\|\boldsymbol{u}_a - \boldsymbol{u}_h\|_{L^2}$	Rates
$1/2$	$5.5e-03$	
$1/4$	$1.5e-03$	1.9
$1/8$	$3.9e-04$	2.0
$1/16$	$1.1e-04$	1.8
Rate	1.9	
Optimal	2.0	

Even though, the results in Table 4.7 achieves almost $\mathscr{O}(h^2)$, the convergence rates still decrease between mesh size $1/8$ and $1/16$. This issue was resolved when choosing $\mathbb{P}_2$ elements for approximating $\boldsymbol{u}$. Here, we set $\nu = 0.4999$, and chose $\mathbb{CG}_2$ elements. These elements have one additional node on each edge in comparison to $\mathbb{CG}_1$ element. We recall that Figure 3.1(a) illustrates the $\mathbb{CG}_1$ element as a triangle. Furthermore, in Table 4.8 we can observe the difference in convergence rate for $\mathbb{CG}_1$ and $\mathbb{CG}_2$ elements. $\mathbb{CG}_2$ elements can expect a order of convergence to be greater than $\mathscr{O}(h^2)$.

Table 4.8 Errors and convergence rate for the displacement obtained with the fixed-stress splitting scheme with singularity removal to a test problem with a line source. Comparing the results obtained with $\mathbb{CG}_1$ and $\mathbb{CG}_2$ elements for $\nu = 0.4999$.

h	$\|\boldsymbol{u}_a - \boldsymbol{u}_h\|_{L^2}$ with $\mathbb{CG}_1$	$\|\boldsymbol{u}_a - \boldsymbol{u}_h\|_{L^2}$ with $\mathbb{CG}_2$
$1/8$	$4.1e-04$	$4.3e-04$
$1/16$	$2.3e-04$	$8.7e-05$
Rate	0.8	2.3

Figure 4.7(a)-(b) shows the plots of $p_{r,h}$ and p_h respectively. Further, Figure 4.7(c) shows the plot of the magnitude of $\boldsymbol{w}_{r,h}$, and Figure 4.7(d) shows the plot of the magnitude of $\boldsymbol{w}_h$. Lastly, Figure 4.7(e) shows the plot of the magnitude of $\boldsymbol{u}_h$. The plots were obtained with $\nu = 0.4999$ and the parameters listed in Table 4.5.

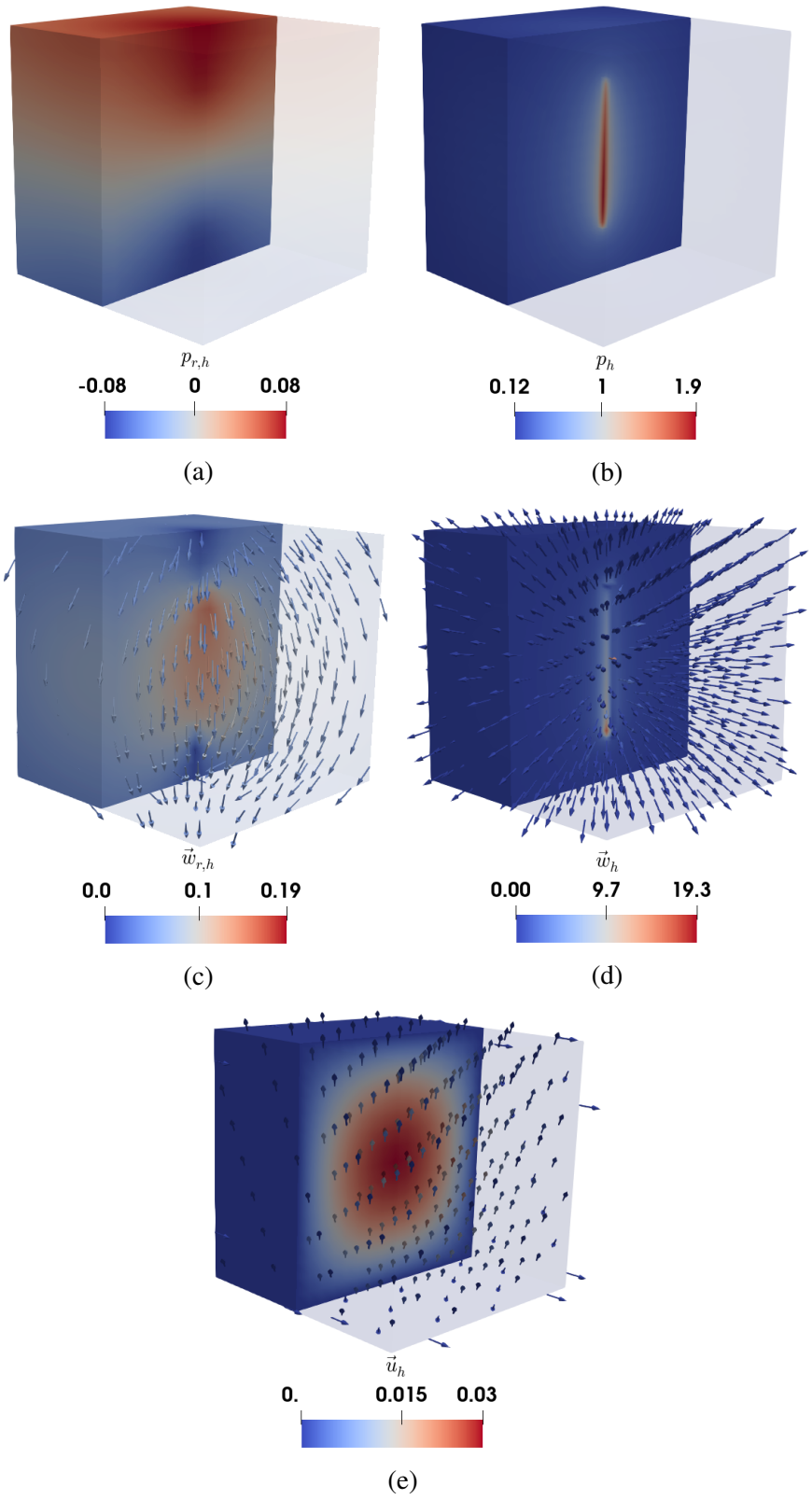

Fig. 4.7 Upper line: Plots of the pressure; the high regularity term (a) and the reconstructed pressure (b). Middle line: Plots of the magnitude of the flux; the high regularity term (c) and the reconstructed flux (d). Lower line: Plot of the magnitude of the displacement; the displacement (e). All plots are numerical solutions obtained by fixed-stress splitting scheme with singularity removal with a line source.

4.2.2 Simulation of flow and mechanics in a non-trivial data set

Finally, we simulated flow and mechanics with a data set describing a vascular system of a human brain. This kind of network is illustrated in Figure 4.8. Here, the red and blue vessels illustrate arteries and veins, respectively. The capillaries are not visualized in this figure, but Figure 1.4 illustrates its structure. The data segmentation and tree extraction were provided by E. Hanson and E. Hodneland.

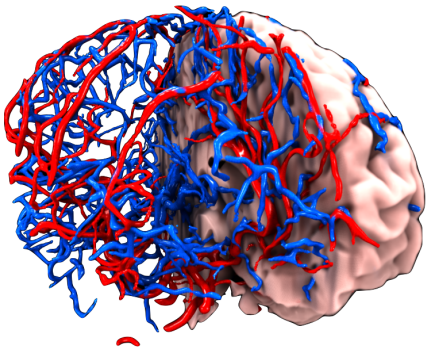

Fig. 4.8 Visualization of a vascular network of a human brain [Hodneland et al., 2019]. The red vessels illustrate arteries and the blue vessels illustrate veins.

We let δ_Γ be m line sources. Here, $m \approx 3000$, and the data set consists of $\Gamma = \cup_{j=1}^{m} \Gamma_j$, where Γ is a collection of m line segments. These line segments represent a vascular system in a human brain. Figure 4.9 shows the data set from the front (a), the side (b) and the top (c). The red lines represent arteries and the blue veins.

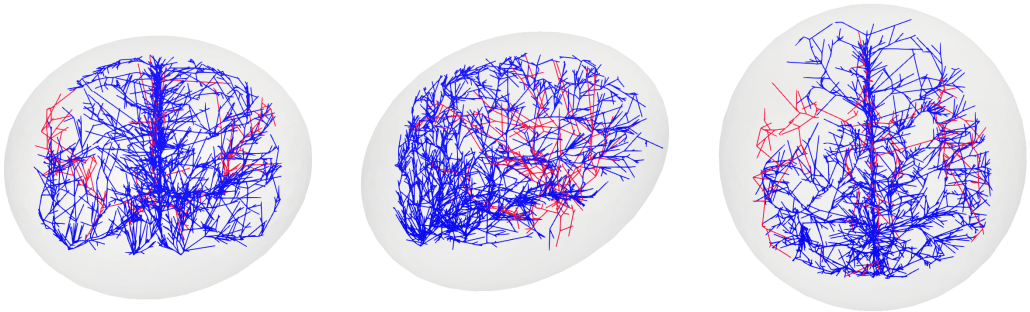

(a) (b) (c)

Fig. 4.9 Illustration of the data set describing a vascular system of the human brain: Front (a), side (b) and overview (c). Here, the arteries (red) and the veins (blue) and the data set consists of ~ 3000 line segments. It was constructed from a MRI scan [Tardif et al., 2016].

The results from these simulations were obtained with the unit cube mesh and the parameters in Table 4.5. We set $\nu = 0.4999$. For the simulation with a non-trivial data, we consider two intensity functions, one for the arteries and one for the veins. We set $f_1 = f(r_{a,j},t)$ and $f_2 = f(r_{v,j},t)$ to be functions of the radii and time for the jth artery and the jth vein, respectively. The line segments are sorted by radii, so we may write:

$$f(r_{a,j},t) = \frac{\sin(t)}{r_{a,j}},$$

$$f(r_{v,j},t) = -\frac{\sin(t)}{r_{v,j}}.$$

The choice of intensity functions is motivated by the fact that blood flows from the arteries through the capillaries and to the veins (before flowing back to the heart). Thus, it makes sense that the arteries are represented as line sources and the veins as line sinks. The motivation for this is that both $f(r_{a,j},t)$ and $f(r_{v,j},t)$ are constants. It also makes sense that the flux increases when the radii become smaller for both the veins and the arteries. In addition, the blood interaction between both the arteries and capillaries, and the capillaries and the veins, are with the smallest vessels of both the arteries and the veins. Hence, it makes sense to set the intensities of the vessels with biggest radii to zero. Since our data set of the veins are the biggest, we set half of the intensities of these line segments to zero. Figure 1.4 illustrates the difference in radius of an artery, a capillary and a vein. Also, the complex structure of a capillary is illustrated.

We look at a closed system, where all the source terms are set to zero. Further, we set the boundary conditions to the flow equations as an arbitrary constant and the mesh was made lager to comply with the boundary conditions. The unit cube mesh was then cropped in ParaView to fit the data set for better visualization. Figure 4.10(a) shows a contour plot of the pressure. Second, Figure 4.10(b) shows the magnitude of the flux. Lastly, Figure 4.10(c) shows the deformation of the domain. Both the flux and the deformation have the direction toward the center of the domain. From a physical point of view, it looks like the brain is shrinking. This means that there is more mass flowing out of the veins than flows into the arteries.

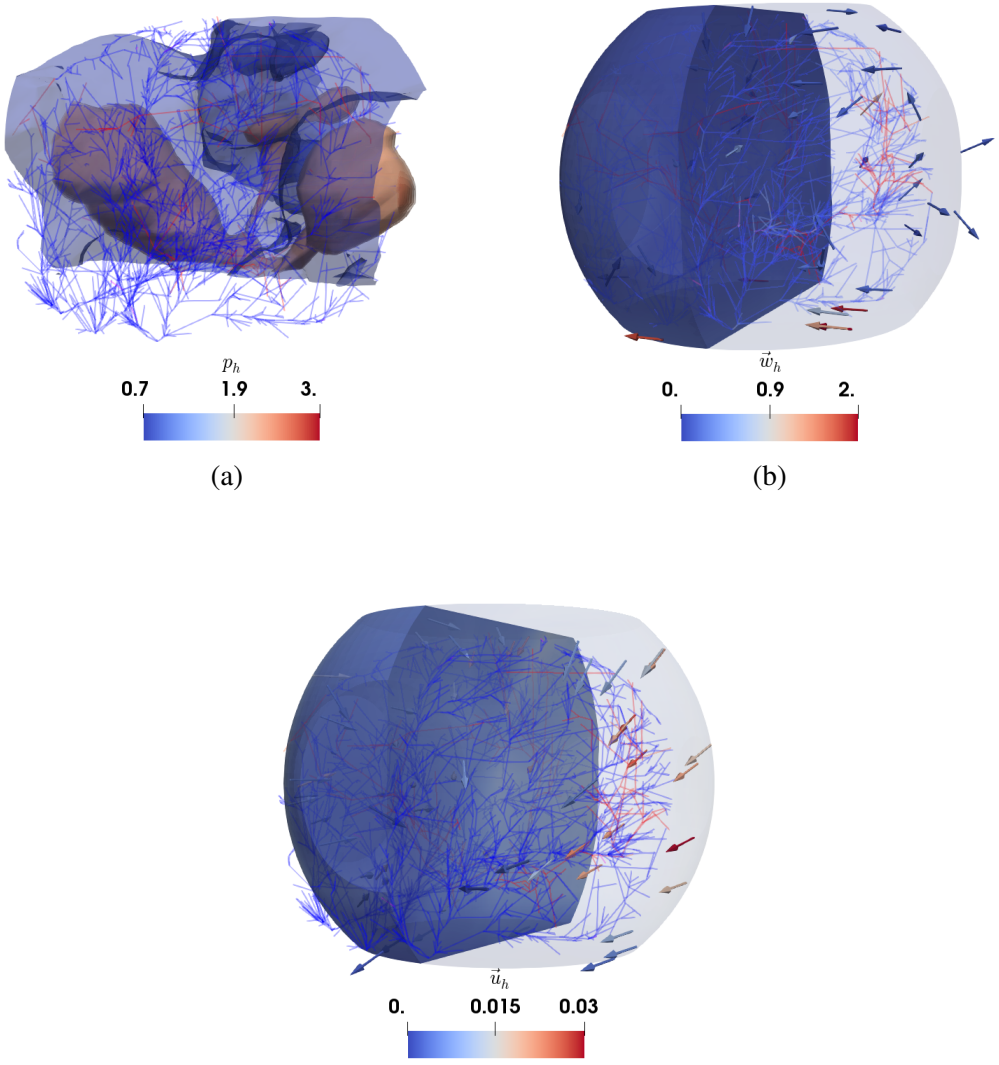

(a) (b)

(c)

Fig. 4.10 The plots are obtained with a data set describing a vascular system of a brain: Contour plot of the pressure (a), magnitude of the flux (b), and the magnitude of the displacement (c). The results are found using the fixed-stress splitting scheme with singularity removal. The data set consists of line segments constructed from a MRI scan [Tardif et al., 2016]. The plots are cropped in ParaView after the simulations to fit the data set.

Chapter 5

Conclusions

In this thesis, we have numerically and theoretically studied the convergence of the fixed-stress splitting scheme for solving the quasi-static, linear Biot model with lower-dimensional source terms. These source terms are modeled as 1D Dirac source terms and cause the solution to be singular at the source point. Central to this work is the observation that a fixed-stress splitting scheme solving the Biot model including such singular source terms leads to a loss of convergence for the flux. In our work, by combining the fixed-stress splitting scheme with singularity removal, we have retrieved the optimal convergence for all variables in our numerical scheme. The scheme is based on splitting the flow solutions of the pressure and the flux in one low, but explicitly-known, term and the other, high regularity, implicitly, term. We then solve the system of equations by the fixed-stress splitting scheme. The explicitly-known low regularity term is then interpolated onto the discrete pressure space to obtain the actual pressure of the problem. It is then used in the mechanics equation to solve the displacement. Thus, the scheme includes one additional step in comparison with the standard schemes. Optimal convergence was proven both theoretically and numerically. We illustrate the approach in several numerical examples including a data set describing a vascular system of a human brain. Our solution scheme treats homogeneous media, but extension to heterogeneous media is straightforward. Moreover, in terms of applications, though we have considered the examples from the biomedical field, other areas such as subsurface processes are equally relevant.

5.1 Future work

For future studies, would be interesting to have a benchmark made for this kind of problem and further investigating results for real applications. In addition to realistic parameters, having more realistic boundary conditions is also of interest. Also, it would be of interest to

perform the simulations on different meshes than the unit square and cube mesh. In particular, a mesh which is similar to the shape of a brain. There would also of interest to extend the convergence tests in Section 4.2.1 to include smaller mesh sizes. Moreover, it can be proved that the scheme has existence and uniqueness as for two academic examples. Also, the proof of convergence can be extended to include heterogeneous porous media, even though this is straightforward. Furthermore, it would be of interest to include a transport equation, for example to describe chemical concentration. Even though this work is a step in the right direction to simulate flow and mechanics in vascular tissue. The problem we should have studied is coupled 1D-3D equations, where the 1D domain Γ is endowed with its own flow equation to simulate flow in vascular tissue [D'Angelo and Quarteroni, 2008].

References

Ahrens, J., Geveci, B., and Law, C. (2005). Paraview: An end-user tool for large data visualization. *Visualization Handbook*.

Almani, T., Kumar, K., Dogru, A., Singh, G., and Wheeler, M. F. (2016). Convergence analysis of multirate fixed-stress split iterative schemes for coupling flow with geomechanics. *Computer Methods in Applied Mechanics and Engineering*, 311:180 – 207.

Alnæs, M. S., Blechta, J., Hake, J., Johansson, A., Kehlet, B., Logg, A., Richardson, C., Ring, J., Rognes, M. E., and Wells, G. N. (2015). The FEniCS project version 1.5. *Archive of Numerical Software*, 3(100).

Armero, F. (1999). Formulation and finite element implementation of a multiplicative model of coupled poro-plasticity at finite strains under fully saturated conditions. *Computer Methods in Applied Mechanics and Engineering*, 171(3):205 – 241.

Armero, F. and Simo, J. C. (1992). A new unconditionally stable fractional step method for non-linear coupled thermomechanical problems. *International Journal for Numerical Methods in Engineering*, 35(4):737–766.

Bause, M., Radu, F., and Köcher, U. (2016). Space-time finite element approximation of the Biot poroelasticity system with iterative coupling. *Computer Methods in Applied Mechanics and Engineering*, 320.

Berger, L., Bordas, R., Kay, D., and Tavener, S. (2017). A stabilized finite element method for finite-strain three-field poroelasticity. *Computational Mechanics*, 60(1):51–68.

Biot, M. A. (1941). General theory of three-dimensional consolidation. *Journal of Applied Physics*, 12:155 – 164.

Biot, M. A. (1955). Theory of elasticity and consolidation for a porous anisotropic solid. *Journal of Applied Physics*, 26(2):182–185.

Borja, R. I. and Alarcón, E. (1995). A mathematical framework for finite strain elastoplastic consolidation part 1: Balance laws, variational formulation, and linearization. *Computer Methods in Applied Mechanics and Engineering*, 122(1):145 – 171.

Borregales, M., Radu, F. A., Kumar, K., and Nordbotten, J. M. (2018). Robust iterative schemes for non-linear poromechanics. *Computational Geosciences*, 22(4):1021–1038.

Both, J. W., Borregales, M., Kumar, K., Nordbotten, J. M., and Radu, F. A. (2017). Robust fixed stress splitting for Biot's equations in heterogeneous media. *Applied Mathematics Letters*, 68:101 – 108.

Both, J. W., Kumar, K., Nordbotten, J. M., and Radu, F. A. (2019). Anderson accelerated fixed-stress splitting schemes for consolidation of unsaturated porous media. *Computers & Mathematics with Applications*, 77(6):1479 – 1502. 7th International Conference on Advanced Computational Methods in Engineering (ACOMEN 2017).

Brun, M. K., Ahmed, E., Berre, I., Nordbotten, J. M., and Radu, F. A. (2019). Monolithic and splitting based solution schemes for fully coupled quasi-static thermo-poroelasticity with nonlinear convective transport. arXiv:1902.05783.

Capurro, M. and Barberis, F. (2014). Evaluating the mechanical properties of biomaterials. *Biomaterials for Bone Regeneration: Novel Techniques and Applications*, pages 270–323.

Castelletto, N., Hajibeygi, H., and Tchelepi, H. A. (2017). Multiscale finite-element method for linear elastic geomechanics. *Journal of Computational Physics*, 331:337 – 356.

Castelletto, N., Klevtsov, S., Hajibeygi, H., and Tchelepi, H. A. (2018). Multiscale two-stage solver for Biot's poroelasticity equations in subsurface media. *Computational Geosciences*.

Cattaneo, L. and Zunino, P. (2014). A computational model of drug delivery through microcirculation to compare different tumor treatments. *International Journal for Numerical Methods in Biomedical Engineering*, 30.

Cerroni, D., Laurino, F., and Zunino, P. (2019). Mathematical analysis, finite element approximation and numerical solvers for the interaction of 3D reservoirs with 1D wells. *GEM - International Journal on Geomathematics*, 10.

Chaabane, N. and Rivière, B. (2018a). A sequential discontinuous galerkin method for the coupling of flow and geomechanics. *Journal of Scientific Computing*, 74(1):375–395.

Chaabane, N. and Rivière, B. (2018b). A splitting-based finite element method for the Biot poroelasticity system. *Computers & Mathematics with Applications*, 75(7):2328 – 2337.

Cheney, W. (2001). *Analysis for Applied Mathematics*, volume 208.

Dana, S. and Wheeler, M. F. (2018). Convergence analysis of fixed stress split iterative scheme for anisotropic poroelasticity with tensor Biot parameter. *Computational Geosciences*, 22(5):1219–1230.

D'Angelo, C. and Quarteroni, A. (2008). On the coupling of 1D and 3D diffusion-reaction equations: Application to tissue pefusion problems. *Mathematical Models and Methods in Applied Sciences*, 18.

Dewhirst, M. W. and Secomb, T. W. (2017). Transport of drugs from blood vessels to tumour tissue. *Nature Reviews Cancer*, 17:738–750.

Dhoat, S., Ali, K., Bulpitt, C. J., and Rajkumar, C. (2008). Vascular compliance is reduced in vascular dementia and not in Alzheimer's disease. *Age and Ageing*, 37(6):653–659.

Ern, A. and Guermond, J. L. (1992). *Theory Practice of Finite Elements*, volume 159.

Evans, L. C. (2010). *Partial Differential Equations, 2nd Edition*.

Formaggia, L., Quarteroni, A., and Veneziani, A. (2009). *Cardiovascular Mathematics: Modeling and Simulation of the Circulatory System*, volume 1.

Gaspar, F. J. and Rodrigo, C. (2017). On the fixed-stress split scheme as smoother in multigrid methods for coupling flow and geomechanics. *Computer Methods in Applied Mechanics and Engineering*, 326:526 – 540.

Gjerde, I., Girault, V., Kumar, K., and Nordbotten, J. M. (2019). A mixed approach to the poisson problem with line sources. (In preparation).

Gjerde, I., Kumar, K., Nordbotten, J. M., and Wohlmuth, B. (2018). Splitting method for elliptic equations with line sources.

Grinberg, L., Cheever, E., Anor, T., Madsen, J. R., and Karniadakis, G. E. (2010). Modeling blood flow circulation in intracranial arterial networks: A comparative 3D/1D simulation study. *Annals of Biomedical Engineering*, 39:297–309.

Helmig, R. (1997). *Multiphase flow and transport processes in the subsurface: a contribution to the modeling of hydrosystems*.

Hodneland, E., Hanson, E. A., Sævareid, O., Nævdal, G., Lundervold, A., Munthe-Kaas, A. Z., Deistung, A., Reichenbach, J. R., and Nordbotten, J. M. (2019). A new framework for assessing subject-specific whole brain circulation and perfusion. PLOS One (to appear).

Hu, X., Rodrigo, C., Gaspar, F. J., and Zikatanov, L. T. (2017). A nonconforming finite element method for the Biot's consolidation model in poroelasticity. *Journal of Computational and Applied Mathematics*, 310:143 – 154.

Khaled, A.-R. and Vafai, K. (2003). The role of porous media in modeling flow and heat transfer in biological tissues. *International Journal of Heat and Mass Transfer*, 46:4989–5003.

Kim, J., Tchelepi, H., and Juanes, R. (2011). Stability and convergence of sequential methods for coupled flow and geomechanics: Drained and undrained splits. *Computer Methods in Applied Mechanics and Engineering*, 200(23):2094 – 2116.

Köppl, T., Vidotto, E., and Wohlmuth, B. (2016). A local error estimate for the poisson equation with a line source term. In Karasözen, B., Manguoğlu, M., Tezer-Sezgin, M., Göktepe, S., and Uğur, Ö., editors, *Numerical Mathematics and Advanced Applications ENUMATH 2015*, pages 421–429, Cham. Springer International Publishing.

Llau, A., Jason, L., Dufour, F., and Baroth, J. (2016). Finite element modelling of 1D steel components in reinforced and prestressed concrete structures. *Engineering Structures*, 127:769–783.

Matthies, G. and Tobiska, L. (2007). Mass conservation of finite element methods for coupled flow-transport problems. *Int J Comput Sci Math*, 1.

Mikelić, A., Wang, B., and Wheeler, M. F. (2014). Numerical convergence study of iterative coupling for coupled flow and geomechanics. *Computational Geosciences*, 18(3):325–341.

Mikelić, A. and Wheeler, M. F. (2013). Convergence of iterative coupling for coupled flow and geomechanics. *Computational Geosciences*, 17(3):455–461.

Morris, J. (2009a). . simulations of injection-induced mechanical deformation: A study of the in salah CO2 storage project. *SEG 2009 Summer Research Work CO2 Seq Geophy, Banff Canada, 23-27 Aug*.

Morris, J. (2009b). Injection and reservoir hazard management: The role of injection-induced mechanical deformation and geochemical alteration at in salah CO2 storage project. *Lawrence Livermore National Laboratory*.

Nabil, M. and Zunino, P. (2016). A computational study of cancer hyperthermia based on vascular magnetic nanoconstructs. *Royal Society Open Science*, 3:160287.

Nordbotten, J. M. (2016). Stable cell-centered finite volume discretization for Biot equations. *SIAM Journal on Numerical Analysis*, 54(2):942–968.

Nordbotten, J. M. and Celia, M. A. (2011). Geological storage of CO2: Modeling approaches for large-scale simulation. pages i–ix.

Park, K. C. (1983). Stabilization of partitioned solution procedure for pore fluid-soil interaction analysis. *International Journal for Numerical Methods in Engineering*, 19(11):1669–1673.

Penta, R., Ambrosi, D., and Quarteroni, A. (2014). Multiscale homogenization for fluid and drug transport in vascularized malignant tissues. *Mathematical Models and Methods in Applied Sciences*, 25:79–108.

Phillips, P. J. and Wheeler, M. F. (2007). A coupling of mixed and continuous galerkin finite element methods for poroelasticity i: the continuous in time case. *Computational Geosciences*, 11(2):131.

Possenti, L., Casagrande, G., Gregorio, S., Zunino, P., and Costantino, M. (2018). Numerical simulations of the microvascular fluid balance with a non-linear model of the lymphatic system. *Microvascular Research*, 122.

Quarteroni, A., Sacco, R., and Saleri, F. (2007). *Numerical Mathematics*, volume 37.

Radu, F. (2004). *Mixed finite element discretization of Richards' equation: error analysis and application to realistic infiltration problems*. PhD thesis, University of Erlangen-Nuremberg, Germany. http://www.am.uni-erlangen.de/index.php?id=3652.

Reichold, J., Stampanoni, M., Keller, A., Buck, A., Jenny, P., and Weber, B. (2009). Vascular graph model to simulate the cerebral blood flow in realistic vascular networks. *Journal of cerebral blood flow and metabolism : official journal of the International Society of Cerebral Blood Flow and Metabolism*, 29:1429–43.

Rodrigo, C., Gaspar, F. J., Hu, X., and Zikatanov, L. T. (2016). Stability and monotonicity for some discretizations of the Biot's consolidation model. *Computer Methods in Applied Mechanics and Engineering*, 298:183 – 204.

Rodrigo, C., Hu, X., Ohm, P., Adler, J., Gaspar, F., and Zikatanov, L. (2018). New stabilized discretizations for poroelasticity and the stokes' equations. *Computer Methods in Applied Mechanics and Engineering*, 341:467 – 484.

Schrefler, B. A. (2004). Multiphase flow in deforming porous material. *International Journal for Numerical Methods in Engineering*, 60(1):27–50.

Shipley, R. and Chapman, S. (2010). Multiscale modelling of fluid and drug transport in vascular tumours. *Bulletin of mathematical biology*, 72:1464–91.

Showalter, R. and Momken, B. (2002). Single-phase flow in composite poroelastic media. *Mathematical Methods in The Applied Sciences - MATH METH APPL SCI*, 25:115–139.

Storvik, E., Wiktor Both, J., Kumar, K., Nordbotten, J. M., and Radu, F. A. (2018). On the optimization of the fixed-stress splitting for Biot's equations. *arXiv e-prints*, page arXiv:1811.06242.

Støverud, K., Darcis, M., Helmig, R., and Hassanizadeh, S. (2012). Modeling concentration distribution and deformation during convection-enhanced drug delivery into brain tissue. *Transport in Porous Media - TRANS POROUS MEDIA*, 92:119–143.

Tardif, C. L., Schäfer, A., Trampel, R., Villringer, A., Turner, R., and Bazin, P.-L. (2016). Open science cbs neuroimaging repository: Sharing ultra-high-field mr images of the brain. *NeuroImage*, 124:1143 – 1148. Sharing the wealth: Brain Imaging Repositories in 2015.

Thomas, J.-M. (1977). *Sur l'analyse numérique des méthodes d'éléments finis hybrides et mixtes (in French)*. PhD thesis, Université Pierre et Marie Curie, Paris.

Weiss, C. (2017). Finite element analysis for model parameters distributed on a hierarchy of geometric simplices. *GEOPHYSICS*, 82:1–52.

White, J. A. and Borja, R. I. (2008). Stabilized low-order finite elements for coupled solid-deformation/fluid-diffusion and their application to fault zone transients. *Computer Methods in Applied Mechanics and Engineering*, 197(49):4353 – 4366.

Yi, S. (2017). A study of two modes of locking in poroelasticity. *SIAM Journal on Numerical Analysis*, 55(4):1915–1936.

Yi, S. and Bean, M. L. (2016). Iteratively coupled solution strategies for a four-field mixed finite element method for poroelasticity. *International Journal for Numerical and Analytical Methods in Geomechanics*, 41(2):159–179.

Zakerzadeh, R. and Zunino, P. (2015). Fluid-structure interaction in arteries with a poroelastic wall model. *2014 21st Iranian Conference on Biomedical Engineering, ICBME 2014*, pages 35–39.